

**Automated Motion of a Radiation Source for
Testing Micromegas Detectors**

&

**Modeling QGP Flow Coefficients Using a
Particle Transport Model**

Karoline Dapprich

24 July 2019

Advisor:

Professor Jamie Nagle, Department of Physics

Honors Council Representative:

Professor Dan Dessau, Department of Physics

Committee Member:

Dr. Harrison Carpenter, Department of Ecology and Evolutionary Biology

Abstract

This thesis consists of two independent parts. In the first section, an automated system for moving a radiation source for testing micromegas detectors was designed, assembled, and programmed. Micromegas amplify the signal from incident radiation through the ionization of the gas filling the detectors. They are reliable and maintain high accuracy under high incident particle flux conditions, but remain vulnerable to ion backflow, which reduces tracking accuracy. To characterize ion backflow, the current drawn by the detector's drift mesh can be measured. However, due to the current's picoamp scale it is very sensitive to noise and drift, which necessitates a time-consuming process of repeated, alternating measurements with a radiation source present and a control with none present. The work presented here automates the motion of the radiation source using code that is easily integrable into existing data-collection programs, in order to facilitate the measurement of ion backflow in micromegas.

In the second section, a particle transport model is used to examine flow coefficients of quark-gluon plasma. These coefficients describe the modes of flow of the medium produced in collisions of relativistic nuclei. Studies using AMPT, a particle transport model, have shown that lower-order flow coefficients can be produced due to differential particle escape from the medium. This project uses a simplified particle transport model to investigate whether the escape mechanism can contribute to the quadrangular (fourth-order) flow coefficient.

Acknowledgements

Firstly I would like to thank my advisor Professor Jamie Nagle for the opportunity to conduct this research and for guidance over the course of the project. I would also like to acknowledge my other committee members, Professor Dan Dessau, who ran the Honors course which provided much helpful feedback, and Dr. Harrison Carpenter. This project would not have been possible without Craig Joy and the training and advice he provided in the machine shop. My gratitude goes to my parents for their support and their advice in navigating many decisions during my time at CU, and to Jacob for always being open to discussion.

Contents

1	Automated Motion of a Radiation Source for Testing Micromegas Detectors	5
1.1	Introduction	5
1.2	Background	5
1.2.1	Benefits of Micromegas	6
1.2.2	Micromegas operating principle	7
1.3	Motivation	9
1.3.1	Ion Backflow	9
1.3.2	Measuring Ion Backflow	9
1.4	Project Goal	10
1.5	Design Considerations	10
1.5.1	Specifications	10
1.5.2	Ease of Use	10
1.6	Apparatus	11
1.6.1	Hardware	11
1.6.2	Electronics	15
1.6.3	LabVIEW Architecture	16
1.7	Conclusion	18
1.7.1	Results	18
1.7.2	Future Recommendations	21
2	Modeling QGP Flow Coefficients Using a Particle Transport Model	22
2.1	Introduction	22
2.1.1	Quark-Gluon Plasma	22
2.1.2	Eccentricity and Anisotropic Flow	22
2.1.3	Models Describing Flow	24
2.2	Research Question	25

2.3	Simulation Methods	25
2.3.1	Initial Conditions	26
2.3.2	Particle Survival	26
2.4	Results	28
2.5	Discussion	29
Appendices		31
A Circuit Diagram		32
B Drawings		33
C Instructions		38
C.1	Assembly	38
C.1.1	List of Parts	41
C.1.2	Assembly Diagram	42
C.2	Use	43
C.3	Building Custom SubVIs	45

Chapter 1

Automated Motion of a Radiation Source for Testing Micromegas Detectors

1.1 Introduction

1.2 Background

Particle accelerators such as the Large Hadron Collider (LHC) investigate the conditions of the early universe, the standard model, and dark matter and antimatter by colliding particles and examining the collision products [1]. Their flux and energy capabilities are ever-increasing; the High-Luminosity LHC, projected to begin operation in 2026, will have a luminosity (particles per area per time) ten times higher than the current system [2].

As particle colliders become more sophisticated, it is imperative that detector technology keep pace with improvements in the flux and energy that accelerators achieve. Detectors must exhibit good gain, gain uniformity, energy and position resolution, be stable and not vulnerable to aging, and operate within a reasonable regime of voltage and signal amplitude [3]. In experiments at the LHC and at the Relativistic Heavy Ion Collider (RHIC) at Brookhaven National Laboratory, time projection chambers (TPCs; Figure 1.1) are used to create three-dimensional reconstructions of particle tracks. The flat ends of these cylindrical chambers are covered by detectors which read out charge and make it possible to determine the position and momentum of incoming particles. An electric field along the length of the TPC accelerates particles towards the detectors, and a parallel magnetic field bends

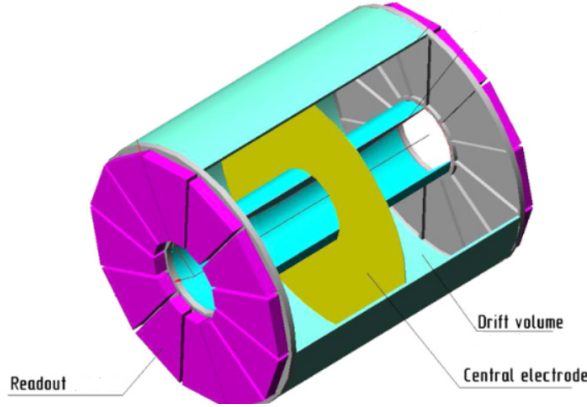


Figure 1.1: TPC schematic from the NICA detector. The diameter of this TPC is approximately 1.1 m. Gaseous ionization detectors cover the pink regions on the ends (figure modified from [7]).

the tracks of charged particles so that momentum can be measured. Micromegas (MICRO-MESh Gaseous Structures) are a type of high-rate detector which are commonly used with TPCs, including at the LHC and CERN’s ongoing upgrade of its ATLAS experiment [4, 5]; they are also proposed for use in the future International Linear Collider and International Large Detector TPCs [6].

1.2.1 Benefits of Micromegas

Micromegas are a common choice for use in detectors utilizing beams from high-flux, high-energy accelerators due to their reliability, good resolution, and high counting-rate capabilities. Their resistance to sparking, which can cause dead time in the signal readout and damage the electronics [8], and aging [9, 10], along with their reliable performance in the high magnetic fields used in TPCs [11] means they can operate successfully for a long time with little maintenance. In addition, they are easily manufacturable to cover 50 cm diameter TPC ends [12]. In high-luminosity environments, micromegas perform well with a counting rate of up to 20,000 counts per second per square centimeter [13] and a time resolution of 10 ns [14]. Likewise they are capable of maintaining good energy resolution under conditions in which a high beam energy results in the detector seeing a high flux of collision products [10, 15]. Their position resolution can be within 70 microns [14, 16]. The maturity and success of micromegas technology make them a leading choice for new high-energy, high-flux experiments, and studies are underway to test their performance under these conditions (e.g.

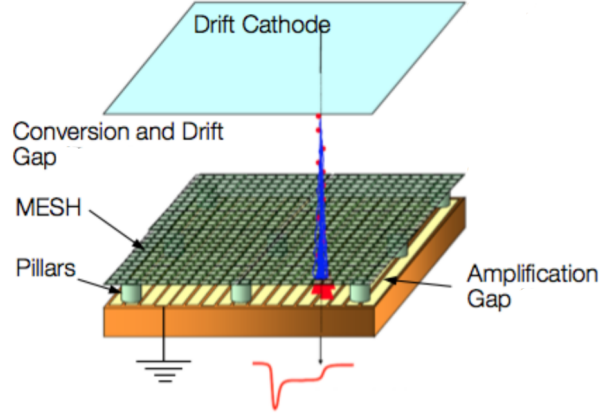


Figure 1.2: Schematic of a micromegas. The electron is incident on the cathode and is accelerated, causing a shower of electrons from the amplification gap to hit the readout electronics (figure modified from [17]).

references [8, 14, 17, 18]).

1.2.2 Micromegas operating principle

Micromegas are parallel-plate detectors belonging to the category of gaseous electron multipliers. When an electron strikes a micromegas, it travels through a gas-filled region, knocking electrons out of the gas molecules it strikes. As these are accelerated by an electric field, they knock out more electrons in a Townsend avalanche until the amplified signal reaches a readout plate on the back of the detector and is recorded.

The micromegas consist of a cathode, metal micromesh, anode, and readout electronics stacked together, with the mesh separated from the readout by narrow, non-conducting pillars (Figure 1.2). The entire system contains a gas mixture, usually of argon acting as the “carrier” gas, which is ionized, and isobutane and CF_4 comprising the “quencher” gases, which are responsible for absorbing UV photons released in the avalanche [19]. The drift region, or drift gap, is the region between the cathode and micromesh and is usually several millimeters wide [17]. It contains an electric field of around 200 V/cm [19]. This lightly accelerates the electron, and very few gas molecules are ionized in this part. Upon reaching the mesh, the electrons are funneled into the amplification region, or amplification gap, which is the area between the micromesh and the anode. The amplification gap is small and contains a high electric field compared to the drift gap—it is only about 100 microns wide [17] and has an electric field on the order of 50 kV/cm [19]. It is in this region where a

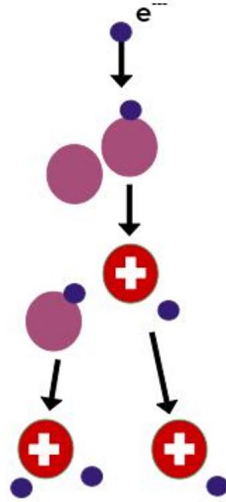


Figure 1.3: Townsend avalanche. An electron strikes a gas molecule, ionizing it. As more electrons are expelled, the avalanche expands.

Townsend avalanche (Figure 1.3) is created as the incident electron is strongly accelerated and ionizes gas molecules; the expelled electrons also ionize the gas, amplifying the signal until all the electrons hit the readout electronics on the anode.

The purpose of the mesh is twofold; it makes it possible to have different electric fields in the drift and amplification regions and it catches ions created in the avalanche. Because the ions are positively charged, their tendency is to drift towards the cathode. However, this distorts the electric field unpredictably and is to be avoided. The mesh, with a pitch of tens of microns [20], mitigates this problem by collecting the ions as they flow back. It remains transparent to electrons, however, because they are smaller and diffuse more [19]. Using a high field ratio makes the mesh even more transparent to electrons; this is also beneficial because a higher amplification field means higher gain.

The readout electronics are pixelated with a pitch of several hundred microns [17], and are often covered with a resistive foil. This foil is designed to reduce the chance of sparking between the anode and micromesh; this works because the field induced in the foil opposes the field from the spark that caused it [14]. This avoids damage to the electronics and dead time which occurs when recovering from a spark, but does not affect the gain of the detector [16]. The resistive foil also increases position resolution, as an incident electron induces a field in the foil, spreading the signal out over several readout pads. This signal can then be localized using an algorithm, making the position resolution better with the foil than without [21].

1.3 Motivation

1.3.1 Ion Backflow

While micromegas perform reliably under high incident particle rate conditions and are not so vulnerable to problems such as sparking, they are still susceptible to ion backflow (IBF). This phenomenon occurs when ions produced in the avalanche are pulled towards the cathode, bringing them into the drift region of the TPC and distorting the electric field within. It is defined as

$$IBF = \frac{N_b}{N_t} \quad (1.1)$$

where N_t is the average total number of ions produced in the avalanche and N_b is the average number of backflowing ions [19]. The field created by these backflowing ions alters the tracks of subsequent electrons in an unpredictable way, introducing error into track reconstructions [19]. This is especially problematic because the way in which the field is distorted is difficult to calculate precisely. In addition, the heavy, slow ions are difficult to quickly evacuate from the chamber, making it impossible to evacuate during high event-rate applications and causing an effect which builds up over the course of the experiment [19]. While there is always IBF in an experiment and it can be corrected for, if the effect is too large it may not be possible to achieve the desired energy and momentum resolution. In general it is beneficial to reduce the amount of IBF, no matter its scale.

Due to the micromesh, micromegas are one of the better technologies at avoiding ion backflow. The mesh collects most of the ions [3], and in some cases one or two additional meshes, called drift meshes, are added in the drift gap to further gate the ions. The scale of ion backflow is small, with the ratio of backflowing ions to total ions produced on the order of 10^{-2} to 10^{-1} [22]. However, the International Large Detector requires IBF to be below 10^{-3} [6], requiring more methods of reducing it. In addition to the use of meshes, IBF can be reduced through the choice of field ratio between the drift and amplification fields, the choice of gas to fill its volume, the mesh pitch, and the size of the amplification gap. However, there are trade-offs to many of these methods; for example, a smaller amplification gap means less IBF but also lower gain [3].

1.3.2 Measuring Ion Backflow

To characterize IBF and gain insight into how it affects the environment of a TPC, the first step is to understand its scale. This can be done by measuring the current drawn by the micromesh as it collects ions (if a drift mesh is used, the current on it should also be measured; this accounts for the contribution from ions produced between the drift mesh and micromesh or the drift mesh and cathode [19]). The current drawn by the mesh is on

the scale of picoamps [4, 23], a very small current that is incredibly sensitive to noise and drift over time. Because of the tiny scale, equipment to measure this current is hard to find, and many repeated, alternating measurements between a control (with no radiation source present) and the test (with a radiation source present) are needed. Alternating test conditions ensures that as the current drifts up or down over time, the data will not be biased.

1.4 Project Goal

In order to characterize IBF, it must be measured; this is complicated by its low magnitude, which makes repeated measurements necessary to correct for drifting. This is a time-consuming process, since a researcher must repeatedly move a radiation source throughout the long testing period. The goal of this project is to create an automated system to move the radiation source used to test micromegas. This will obviate the need for continuous involvement of the researcher and allow test configurations to be reliably repeated.

1.5 Design Considerations

1.5.1 Specifications

The final system must be automated, with code integrable into an existing LabVIEW environment, which already controls the high voltages and IBF readout system. It must support an Fe-55 radiation source, which can be shuttered for doing control tests and be able to move along one axis so that varying intensities can be tested. The prototype micromegas chambers which will be tested are 10 cm^2 . Lastly the entire system must be able to be disassembled for shipment to France for use at the Saclay Nuclear Research Center.

1.5.2 Ease of Use

In addition to the required specifications, design considerations concerning the ease of use and reliability of the apparatus are also important. To make operation intuitive, the user enters the distance the source should move, not the number of steps the motor needs to take to go that far. The position of the source is always displayed and there is a warning message should the user enter a distance which would put the source outside of its allowed range. Preset routines allow the user to start the system and leave it to complete a set sequence of motions; these can be custom-built and added to the code. To ensure repeatability in testing and accuracy in calculating position, there is a zeroing mechanism. Should there be a problem with the zeroing or position tracking, hard stops at both ends of the axis of

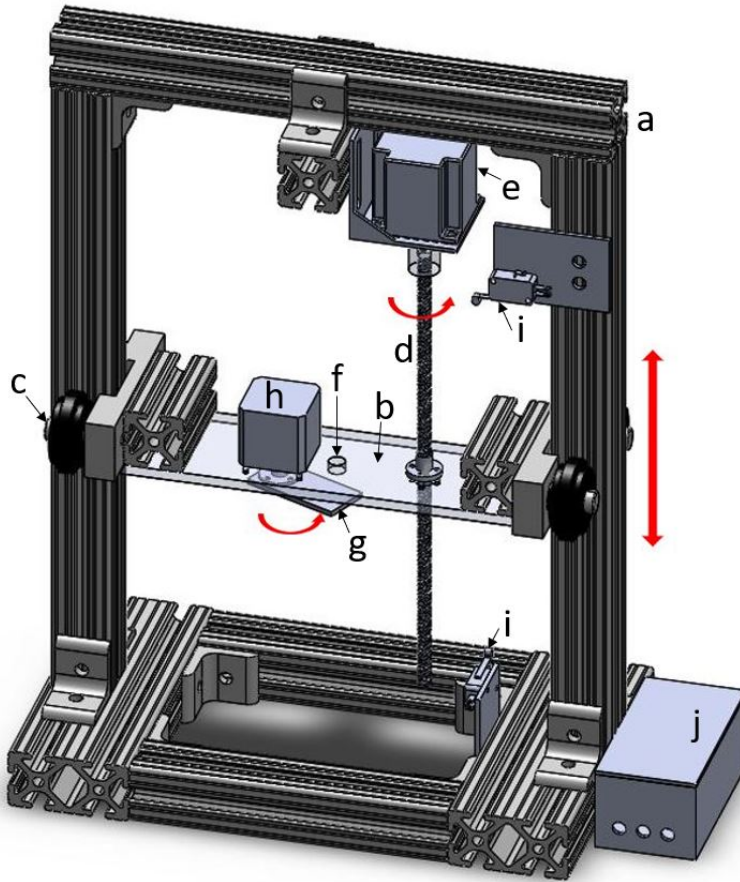


Figure 1.4: Model of apparatus, 8 x 11 x 18 in (approximately 20 x 28 x 46 cm). The micromegas is placed in the base and irradiated by an Fe-55 source placed over the hole in the platform (f). A lead screw (d) drives vertical motion of the platform.

motion prevent damage to the apparatus and the tile being tested. Guides are included for assembly, use, and creation of preset routines (Appendix C).

1.6 Apparatus

1.6.1 Hardware

Complete drawings of the apparatus were made using SolidWorks [24] and can be found in Appendix A. An assembly guide (Appendix C.1) will make setup straightforward. The main assembly (Figure 1.4) is supported by a T-slot aluminum frame (a), which has a T-shaped

groove on each side. This makes it very versatile because it is easy to bolt things together by sliding nuts into the grooves, or to make a track for wheels which fit into the slots. In this project, an aluminum platform (b) rides on wheels (c) along the vertical supports and is moved by a lead screw (d) attached to a NEMA 23 stepper motor (e) [25]. This motor is mounted above the platform on the horizontal crossbar of the frame. The Fe-55 radiation source will be placed on the platform over a hole (f) in its center, which can be opened or closed by means of a rotating shutter (g) powered by a NEMA 17 stepper motor (h) [26]. Limit switches (i) trigger when the platform depresses their lever, allowing the position to be zeroed to ensure repeatability. All circuitry is enclosed in a box (j) which has ports to connect to a power supply unit and a USB (electronics will be further discussed in Section 1.6.2).

Stepper motors were used both to drive the linear motion of the platform and to rotate the shutter. They operate by moving a discrete number of steps, making position tracking easier than with servo motors, which rotate continuously and require an optical encoder to track position. Steppers are also less expensive and better suited to loads such as this one which require little acceleration [27]. Inside a stepper motor, there are two concentric magnetic rotors which are aligned to have alternating north and south poles. Around this are four wire coils with their axes aligned with the rotors' diameter. The set of two coils facing each other is called a phase. By supplying current through a phase, magnetic fields are created, pulling the rotors to align with the field. By switching on one phase, then the other, the motor can be pulled through a full rotation in a series of discrete steps [28]. In a bipolar motor, used here, the direction of the current through the windings can be switched, meaning that all coils can be energized at once for higher torque [29]. In this project, two-phase bipolar motors with 200 steps per revolution were used for both the shutter and linear actuator. The shutter does not require as much power as the stepper provides; however, the initial design using a simple rotary actuator was not successful. The actuator required power to remain in the closed position and would overheat quickly when closed, causing it to open unreliably.

The shutter under the radiation source is made of a 1/8" (3.175 mm) thick piece of aluminum. This is sufficient to stop the 5.2 keV electrons radiated by the Fe-55 source, which travel about 15 mm in air and 0 mm in biological tissue [30]. The size of the shutter was calculated such that at the minimum plate height, the shutter blocks radiation from the entire radius of where the micromegas is. This resulted in a minimum diameter of 1.14 in (2.89 cm).

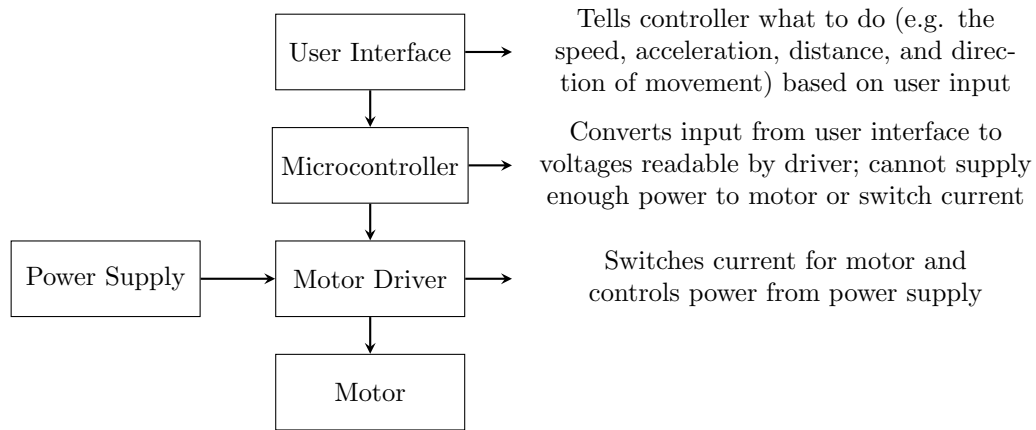


Figure 1.5: The functions of the user interface, Arduino microcontroller, and H-bridge motor driver are distinct.

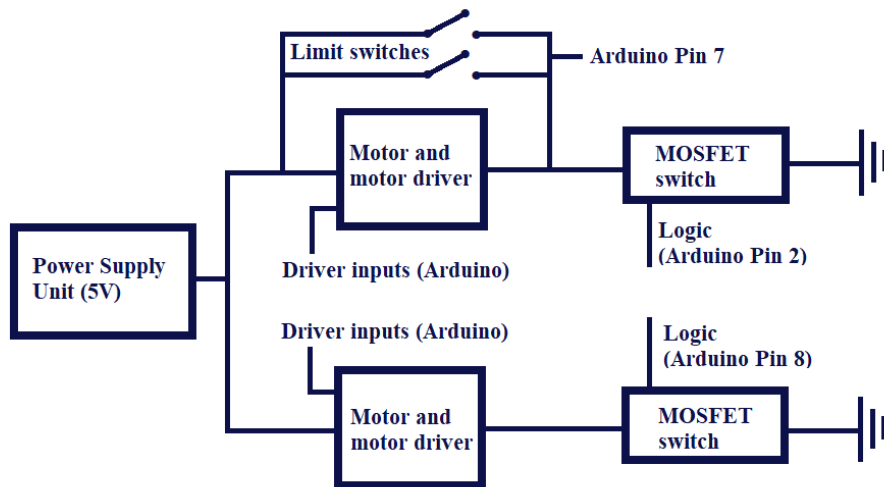


Figure 1.6: Electronics block diagram. The Arduino microcontroller communicates with LabVIEW via a USB connection. A complete circuit diagram is available in Appendix A.

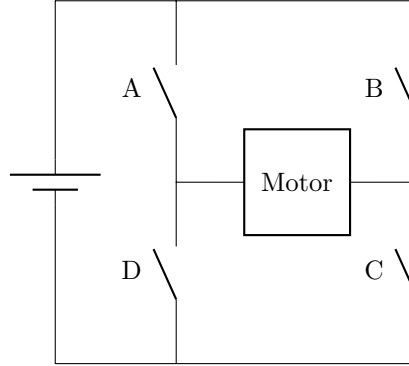


Figure 1.7: H-bridge schematic. By closing either gates A and C or gates B and D, the direction of the current through the motor can be reversed. Each phase of the stepper motor is driven by one H-bridge.

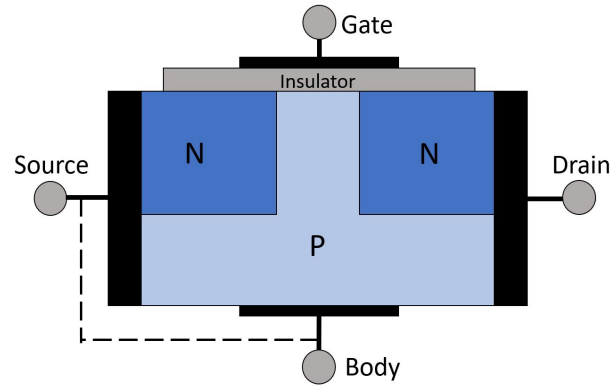


Figure 1.8: MOSFET schematic. “N” and “P” refer to positively and negatively doped semiconducting regions. In an enhancement-mode MOSFET, when $V_{ds} > 0$ and $V_{gs} = 0$, the channel does not conduct. When a gate voltage is applied, the electric field produced in the semiconductor between the gate and body electrodes causes charge carriers to build up on the surface of the insulator, “enhancing” the channel. These charges then travel between the drain and the source due to V_{ds} , turning the switch on (figure based on [31]).

1.6.2 Electronics

An Arduino Uno [32] was chosen as the microcontroller because it is compatible with all the components including LabVIEW [33], with which it communicates through a USB connection. The Arduino can receive directions from LabVIEW as well as transmit information to it. For example, the limit switches [34] are normally open, but when depressed they conduct current which is read by the Arduino and signals the program to move to the next step in the zeroing protocol. Along with a controller, a motor driver is required to be the intermediary between the motor and the power supply as well as between the motor and the controller (Figure 1.5). The Arduino cannot supply enough power to the motors or switch the current; it is limited to a range of +5 V to 0 V on each pin. To drive the motor, the driver takes commands from the controller and supplies the appropriate current to the motor. A block diagram of the circuit is shown in Figure 1.6.

In this project, H-bridge circuits [35, 36], which switch the polarity of an applied voltage, are used to drive the stepper motors. An H-bridge contains four switches (enabled according to input from the controller) connected to a central load (Figure 1.7); by closing two at a time, the direction of the current through the motor can be controlled. For example, in Figure 1.7, closing switches A and C allows current to flow from left to right through the motor, while closing switches B and D allows current to flow from right to left [37]. The H-bridge components used here each contain two such circuits, one for each winding in the motor.

To prevent overheating, the power supply unit is limited to 5 V and 1 A, which is enough power for logic and motion. In addition, MOSFET-based switches turn power on and off when either motor moves [38]. A MOSFET, or metal oxide semiconductor field-effect transistor, has three pins: gate, drain, and source (Figure 1.8). The gate-to-source voltage acts as logic, enabling or disabling current to flow between the source and drain. The current flows through a semiconductive channel, which in an enhancement mode MOSFET (used here) is non-conductive, or normally open, by default. The gate electrode, together with an internal body plate (often connected to the source), acts as a capacitor; when a voltage is applied to the gate, an electric field is produced across the channel, causing charge carriers to accumulate on a metal oxide insulator adjacent to the gate. This is known as enhancement of the channel and enables it to conduct. By applying a voltage between the source and drain, an electric field perpendicular to that created by the gate is produced, and the free charges are pulled in one direction, creating a current [31].

When a motor is moving, the current is switched through the coils every time the motor takes a step; while this current must be within the limits of the driver, the inductance of the coils prevents the current from getting very high. In contrast, if the power is not cut off when the motor is stationary, the motors continue to draw current because the circuit is

still closed and the only resistance is that of the windings. This enables them to hold, for example, a heavy load in a given vertical position without rotating and letting it slipping downwards. However, this idle current is present whether or not a high holding torque is required. For the NEMA 17 motor, a resistance of $1.1\ \Omega/\text{phase}$ [25] combined with the SN754410 H-bridge's maximum voltage output of $3\ \text{V}/\text{pin}$ [35] leads to an idle current of $2.73\ \text{A}/\text{phase}$, which is above the H-bridge's rated maximum continuous output of $1\ \text{A}$. Since the idle current was not needed to maintain the position of the shutter or the platform in this project, shutting off power keeps the current within the driver's limits and does not affect the device's performance. Because the NEMA 23 motor runs for much longer periods than the smaller motor controlling the shutter, an L298 H-bridge [36] was used as its driver. The L298 has a maximum continuous current rating of $2\ \text{A}$ and is therefore less vulnerable to overheating than the SN754410, whose performance suffered even when operating within its rated limits for extended periods of time.

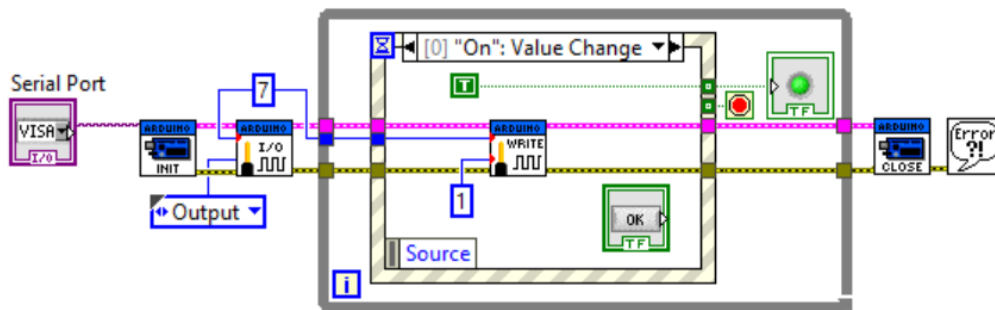
1.6.3 LabVIEW Architecture

LabVIEW is a graphical programming language that contains a front panel (Figure 1.9a), which is the user interface, and a block diagram (Figure 1.9b), which contains the code, in each program. A program is called a virtual instrument or VI because the user interacts only with controls and indicators on the front panel; the VI can control equipment, follow procedures, and take data, making interacting with it very similar to using a regular piece of equipment such as an oscilloscope. In the block diagram, data flow is controlled by wires between subVIs, which are equivalent to functions called by a main program in a text-based language. For this project, LabVIEW Interface for Arduino (LIFA) [39] was used because it has a well-developed library of stepper motor functions. At this time, LIFA is no longer supported and has been replaced by LINX. While moving to LINX would ensure up-to-date documentation, LINX does not have a library of stepper functions, which means that an entire set of custom commands would have to be built. LIFA, though not supported, makes sense for stepper motor projects in LabVIEW for this reason.

In the program developed for this project, subVIs were used for all functions (discussed below) in order to make the code easier to understand and troubleshoot. The front panel has controls to run each function and locks while a function is executing to avoid position miscounting or movement errors. It also always displays the current position of the radiation source for the operator's reference. When a button on the front panel is pressed, it is registered by an event structure in the block diagram. Using an event structure prevents the program from constantly polling the front panel to check for an event, as it would were a while loop monitoring the button, improving code performance. In addition, this structure



(a) Front panel



(b) Block diagram

Figure 1.9: An example of a LabVIEW program which operates a switch. The user interacts only with the front panel (a), while the block diagram (b) contains all the code.

keeps control with the main program, not the subVIs, avoiding possible race conditions. Throughout the program, all motion is automatically preceded by turning on power to the motors and is succeeded by cutting power. A wait time is built in to power-on to ensure that applied voltages have time to reach their full value before the VI executes the next step.

The main program includes subVIs for the following functions:

- Turn shutter: opens and closes shutter over radiation source
- Zero: zeros machine by registering an event when a limit switch is triggered
- Move: allows user to set speed and distance of travel
- Return to start: moves source back to default position at top
- Buildable preset functions: allow user to design a routine and add it to the main VI
- Exit program: safely exits the main VI

The zeroing protocol and custom routines use a state machine architecture, which executes commands in an order determined by the outcome of the previous state. This means the program is more flexible than a similar sequence structure; it is also easier to read and understand on the block diagram. Additionally, the state machine only needs to monitor the limit switches during certain steps, speeding up the program. Preset routines can be designed using any available subVIs and added to the main VI by following the guide (Appendix C.3). This allows the user to set test parameters such as duration, source location, and sequence of tests, then leave the system to run. In the Move function, if the user enters a distance that will put the platform outside its allowed range, the program will not move but instead display an error message containing the distances the platform is allowed to move. Both this function and the Return to Start function make use of a step-counting system which tracks the current position by using input from every subVI that moves the main platform.

1.7 Conclusion

1.7.1 Results

The current design of the apparatus (Figure 1.10) is compromised by uneven motion of the platform. The platform is pulled by the lead screw near the center, but not directly in the center. Combined with the weight of the platform and the NEMA 17 motor, this makes the platform unbalanced and causes it to lean slightly. Despite this, it rides smoothly until

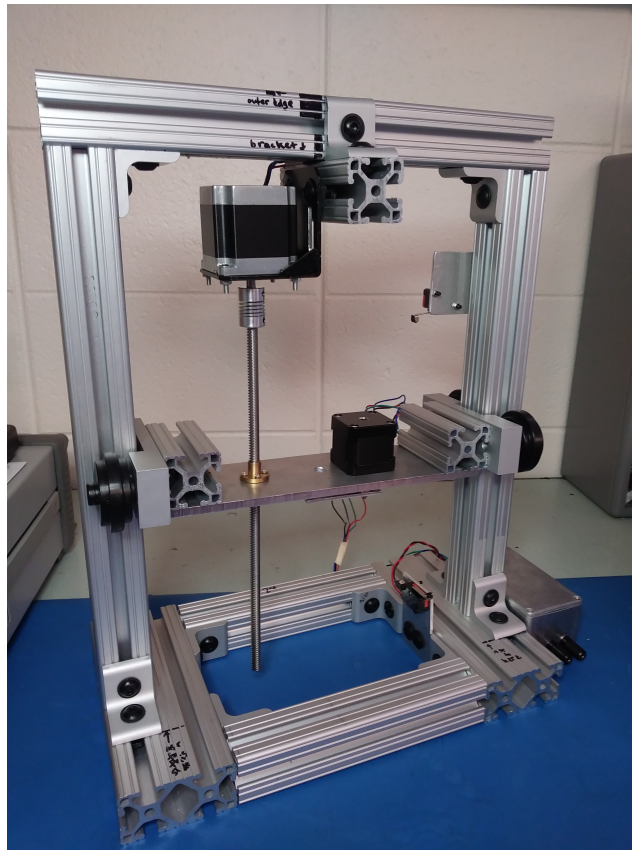


Figure 1.10: Manufactured device



Figure 1.11: As the platform gets higher, the coupler bends due to the torque from the platform, even if the lead screw and motor shaft were initially aligned.

it reaches about 150 mm above its lowest position, at which point it begins to chatter. Traveling at or under 100 steps/second when moving beyond this position alleviates the problem somewhat. At lower heights, speeds up to about 120 steps/second result in smooth motion. Above 120 mm, the flexible coupler between the NEMA 23 motor and the lead screw begins to noticeably bend and stretch (Figure 1.11). The unevenness of motion overall, and the ranges in which it happens, depend heavily on how well the lead screw is aligned with the NEMA 23 shaft. As the point of attachment of the screw to the platform moves upwards, the angle between the shaft and the screw becomes more acute, causing the coupler to flex until it is too stretched to function correctly. Eventually the platform becomes tilted enough that the lead screw can no longer properly drive it upwards.

Despite the limitations on upward movement, all downward motion of the platform is smooth and does not exhibit the chattering at higher positions. While moving upwards smoothly, the platform remains within 0.5 mm of the calculated position. Once the coupler begins to bend and the platform stutters, however, it can be 5-10 mm below what is displayed by the program. The difference between the actual position and the expected position is explained by the stretching of the coupler. This ability to stretch is meant to make assembly easier, because there is some forgiveness if the screw and shaft are not perfectly aligned. However, in this application, the load on the coupler means the flexibility inhibits motion.

Should the platform move too far downwards or upwards, it will get stuck against the brackets and sustain no damage. However, if it gets stuck, the coupler on the lead screw

should be repositioned as it can get pushed up or down the shaft of the motor depending on which direction the platform was traveling. Since the shutter is not subject to the problems introduced by moving along tracks or by its weight, its motion is highly consistent. The performance of the MOSFET switches, limit switches, Arduino, and code is reliable. The SN754410 H-bridge functions well for the NEMA 17 motor controlling the shutter, but overheats after several minutes if used to drive the NEMA 23. For this reason it was replaced with an L298 H-bridge, which can safely handle twice the amount of current.

1.7.2 Future Recommendations

In a future iteration of this apparatus, there are several things to be improved upon. To increase the number of testing geometries that are possible, motion in two or three dimensions is needed. A rigid coupler between the lead screw and NEMA 23 motor shaft would solve the problems caused by the flexibility of the shaft. Alternatively, placing the motor underneath the platform so that there is no weight on the coupler would keep it continuously compressed and prevent it from flexing. Placing the lead screw in the center of the platform would also help it to move more easily by preventing it from tilting. Placing the motor underneath or moving the lead screw while also keeping the radiation source centered over the tile would necessitate adjustments to the base dimensions. To ensure consistent placement of tiles during tests, a frame can be placed inside the base. This would most easily be accomplished through 3D-printing. To keep better track of position, the current code should be updated to monitor the limit switches continuously when the platform is moving instead of relying on calculated allowed travel distances. This will make the position tracking dependent on the physical system; although the steps of the motor can be reliably tracked solely with code, the position of the platform is subject to more unpredictable effects.

Chapter 2

Modeling QGP Flow Coefficients Using a Particle Transport Model

2.1 Introduction

2.1.1 Quark-Gluon Plasma

In the universe's first microseconds of existence, it consisted of a very hot, dense, low-viscosity fluid of quarks and gluons known as the quark-gluon plasma (QGP) [40]. Today accelerators such as the Relativistic Heavy Ion Collider (RHIC) and the Large Hadron Collider (LHC) create QGP [41] by colliding ions close to the speed of light, at energies on the order of tera-electron volts [42]. As nuclei are accelerated, they are Lorentz contracted into disks only a small fraction of a femtometer thick [40], and as hadrons in the colliding nuclei are broken apart, QGP is formed in the overlapping region. This high-energy region experiences a pressure gradient from its center to its edge, causing it to expand rapidly. The medium expands hydrodynamically until reaching a low enough energy density, at which point it transitions to a collection of hadrons which may scatter off one another before leaving the collision area [40].

2.1.2 Eccentricity and Anisotropic Flow

Particle collisions can be classified by their centrality, or how much the nuclei overlap. Central collisions have a collision area that is almost circular, while in noncentral or peripheral

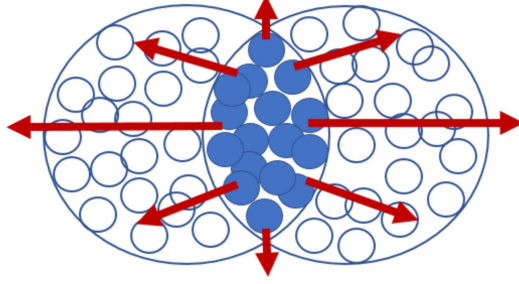


Figure 2.1: An anisotropic collision. The shape of the collision region and the distribution of particles within it contribute to the eccentricity. Red arrows indicate pressure gradients which dictate the speed of expansion.

collisions, the overlapping area is a lenticular shape (Figure 2.1). Combined with the uneven distribution of nucleons within the nucleus and of partons within the nucleons [40], this asymmetric shape gives rise to a quantity called the eccentricity ε_n . The most familiar component of eccentricity is ε_2 , which is the elliptic component. Higher order components such as triangular and quadrangular geometry can also be described, with ε_n given by

$$\varepsilon_n \equiv \frac{\sqrt{\langle r^2 \cos(n\phi_{part}) \rangle^2 + \langle r^2 \sin(n\phi_{part}) \rangle^2}}{\langle r^2 \rangle} \quad (2.1)$$

where ϕ_{part} and r are the polar coordinates in the transverse plane of the participant nucleons [15]. It is important to note that this depends not only on the shape of the collision region, but also on the distribution of particles within it. Therefore even very central collisions can have a non-zero eccentricity. The angular distribution of particles can be described by the Fourier series

$$\frac{dN}{d\phi} \propto 1 + 2\varepsilon_2 \cos(2\phi) + 2\varepsilon_4 \cos(4\phi) + \dots \quad (2.2)$$

Similarly, the momentum distribution of the particles can also be described by the series

$$\frac{df}{d\phi} \propto 1 + 2v_n \cos(2\phi) + 2v_4 \cos(4\phi) + \dots \quad (2.3)$$

where v_n is the n^{th} flow coefficient [43]. Like eccentricity, flow has multiple harmonics, and there are strong relationships between certain components of eccentricity and their corresponding flow harmonics. For example, in ideal hydrodynamics, $v_n \propto \varepsilon_n$. The harmonics are produced due to the anisotropic pressure gradients present in a noncentral collision. Because the medium is not symmetrical, and because the pressure must drop from the maximum at the center to a constant along the edge of the medium, the pressure gradients created are

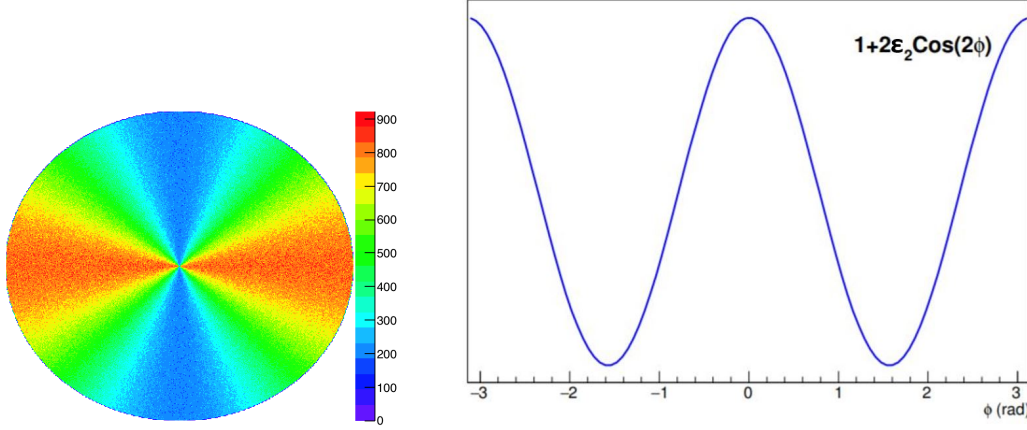
strongest along the minor axes (red arrows in Figure 2.1). This means that, for example, an ellipse will expand fastest along its minor axis, creating elliptical flow in the direction perpendicular to its initial eccentricity [44].

Of the flow coefficients, the elliptic coefficient v_2 is the largest in magnitude [44], and it and the triangular flow coefficient v_3 are well-approximated by a linear dependence on ε_2 and ε_3 , respectively [45, 46]. In contrast, higher flow harmonics are of lower magnitude, and while they contain components linearly proportional to ε_n , they are dominated by contributions from non-linear hydrodynamic responses to the initial eccentricity [45, 46]. This is especially true of peripheral and midcentral collisions, which experience more mode mixing than highly central ones as the large elliptic flow interacts strongly with higher-order modes [44].

2.1.3 Models Describing Flow

The strongly coupled, very low-viscosity QGP fluid has been modeled by relativistic hydrodynamics very successfully, but in many cases models of the QGP as a collection of particles also agree quantitatively with experimental data. For example, a multi-phase transport model (AMPT) can show how initial eccentricity is translated into flow anisotropy [47, 48]. Models such as this include partons scattering off one another before freeze-out (i.e. escape from the collision area), and this was initially believed to be the mechanism through which they generated harmonic flow. Because fluid behavior is expected in the limit of many scatterings, this appeared to make sense; however, it was later shown that the number of scattering events experienced by partons in AMPT is fairly small, and in small systems most partons do not scatter at all [47].

In 2016 He *et al.* showed that the elliptical and triangular flow produced by AMPT resulted from the differential probability of partons to scatter and escape, not the scatterings themselves [41]. This is easily understood by noting that in a QGP distribution with non-zero eccentricity, the probability of a particle escaping depends on both the density of the medium through which it must travel and how far it must travel to escape the medium. This in turn depends on its angle of travel with respect to the medium's major and minor axes, and at what radius from the center of the distribution it starts. Even particles which do not scatter escape from the medium with a positive v_2 as a result of this differential escape probability, and overall the role of multiple scatterings in creating flow harmonics is very small [41]. Thus it is established that for v_2 and v_3 , the probability of parton escape, which is heavily dependent on initial eccentricity, results in anisotropic flow. However, the higher-order harmonics have not been examined with this kind of model; hydrodynamic mode-mixing is the only method by which these effects have been explained.



(a) Initial particle distribution with $\varepsilon_2 > 0$ and $\varepsilon_4 = 0$. Red corresponds to higher particle density and blue to lower. This example uses a total of 10^8 particles and $v_2 = 0.3$.

(b) Function describing particle density with respect to ϕ , $F(\phi) = 1 + 2v_2 \cos(2\phi)$ with $\varepsilon_2 = 0.3$ (Equation 2.4). The magnitude of the function determines the degree of anisotropy in Figure 2.2a, and does not have physical significance by itself.

Figure 2.2: To create the initial distribution (Figure 2.2a), values were randomly pulled from the distribution given by Figure 2.2b.

2.2 Research Question

While hydrodynamic models show how a non-zero v_4 can arise as a response to the initial elliptic eccentricity, whether this can be an effect of parton survival has not been fully studied. This work aims to determine whether a particle model of the QGP can describe the evolution of higher-order flow harmonics from an initial state with only elliptical eccentricity. Specifically, in the absence of scattering, can differential particle survival explain the evolution of a non-zero v_4 from an initial distribution with $\varepsilon_4 = 0$ and $\varepsilon_2 > 0$?

2.3 Simulation Methods

In order to determine whether a v_4 could arise from an initial conditions with $\varepsilon_4 = 0$ and $\varepsilon_2 > 0$, a model was created using ROOT [49] in which particles in an appropriate distribution moved step-wise in random directions through the medium until reaching its edge. Their survival was made dependent on the number of partons encountered along their paths, and the final distribution of surviving partons was fit to Equation 2.3 to determine values of v_2 and v_4 . The ratios of these quantities were then compared to predictions from ideal hydrodynamics as well as measurements from RHIC.

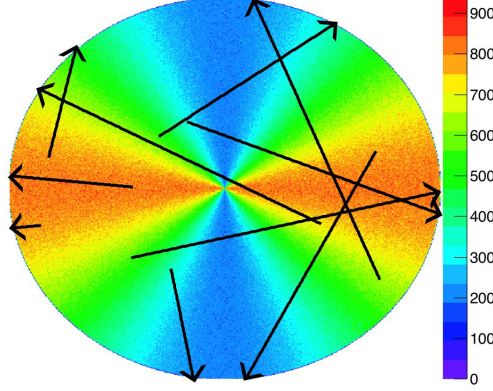


Figure 2.3: The position of particles and the angle at which they travelled through the medium were selected randomly.

2.3.1 Initial Conditions

To create the initial geometry, a 2D circular histogram of radius one, representing the collision area (Figure 2.2a), was randomly filled with 10^6 particles according to the distribution (Figure 2.2b) given by

$$F(\phi) = 1 + 2\varepsilon_2 \cos(2\phi) \quad (2.4)$$

with the parameter ε_2 set equal to either 0.1, 0.2, or 0.3 to control the magnitude of the initial anisotropy. This means the distribution had elliptical eccentricity, but no quadrangular eccentricity; using Equation 2.1, $\varepsilon_2 \approx 10^{-1}$ and $\varepsilon_4 \approx 10^{-4}$. Additionally, since the histogram is a circle, the eccentricity is due entirely to the distribution of particles within the collision area rather than the shape of the area itself. Particles from the histogram were then selected at random and given a random angle (from a flat distribution) at which to travel (Figure 2.3).

2.3.2 Particle Survival

As particles travelled across the collision area, each step was weighted according to the contents of the histogram bin the particle passed through. The weighted path length L was then calculated by summing these weighted distances according to

$$L = \sum_i^N dr * h_i \quad (2.5)$$

where dr is a constant step size and h_i is the content of each bin. To normalize the resulting paths, each path length was divided by a hypothetical maximum possible path L_{max} . This

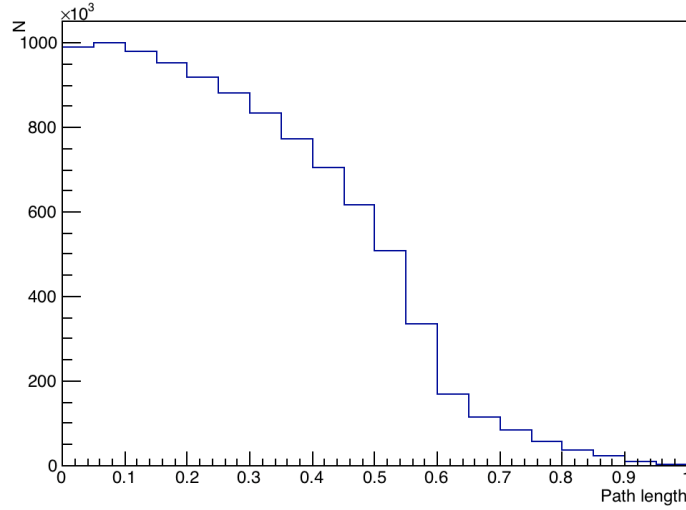


Figure 2.4: Distribution of normalized path lengths of particles travelling through the medium

maximum was calculated by stepping a particle along a diameter from $(-1,0)$ to $(1,0)$, which is through the highest particle density, and weighting each step as before. Although this is almost certainly slightly larger than the actual maximum path, it is close enough to normalize the paths to an intuitive scale (Figure 2.4).

Since the survival of particles depends on how many other particles they encounter before exiting the medium, survival was modeled as a decaying exponential dependent on the weighted path length. Since the angle of travel dictated the density a particle encountered and therefore the weighted path, it is not necessary to include angle in the survival function. The likelihood of a particle surviving was therefore described by

$$Survival = e^{-\lambda \frac{L}{L_{max}}} \quad (2.6)$$

where λ is a scaling parameter. This function was used to weight entries in a histogram binned by travel angle, resulting in a distribution showing the harmonics produced by differential survival. The angle of travel was plotted instead of final angle with respect to the origin because the purpose of the study is to investigate flow coefficients; we care about which direction the particles are going, so they are binned by direction of motion rather than angular position. The elliptic and quadrangular flow coefficients v_2 and v_4 of the resulting distribution were found using a fit to Equation 2.3. The ratios between v_2 and v_4 were then checked against those measured at RHIC, $v_4 = (v_2)^2$, and those predicted by ideal hydrodynamics, $v_4 = \frac{1}{2}(v_2)^2$ [43]. Since the data did not agree with predictions, ROOT was used to examine the relationship produced between v_2 and v_4 .

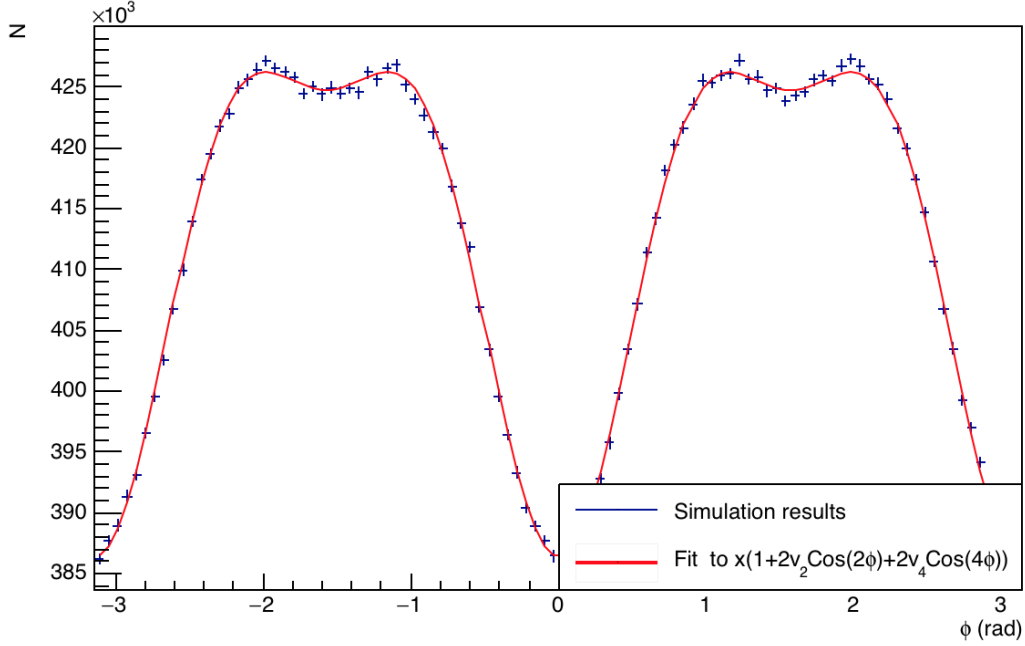


Figure 2.5: Direction of flow for surviving particles. The v_4 contribution is visible in the four maxima present over the 2π range. The parameters for this fit are $v_2 \approx -2 \times 10^{-2}$ and $v_4 \approx -9 \times 10^{-3}$; x is a scaling parameter to account for the high statistics (10^8 particles).

2.4 Results

Differential particle survival resulted in final elliptical and quadrangular flow, although not in the expected ratios. As visible in Figure 2.5, which shows survival as a function of travel angle, quadrangular flow is present but at a small magnitude. Values of v_4 were on the order of -10^{-2} to -10^{-4} (Figure 2.6), depending on the values of λ and the initial degree of anisotropy (ε_2 in Equation 2.4). The coefficients are negative because the dominant directions of flow will be in the direction where the lowest particle density was in the initial distribution. This places the maxima for flow where the minima in the distribution were, which mathematically corresponds to replacing a positive coefficient with a negative one in an equation of the form $1 + v_2 \cos 2\phi$. Despite the presence of both relevant types of flow, the ratios between the two did not match either predictions from ideal hydrodynamics ($v_4 = \frac{1}{2}(v_2)^2$) or data taken at RHIC ($v_4 = (v_2)^2$). There was no predictive relationship between final v_2 and v_4 in this study (Figure 2.6); both a linear and quadratic fit produced χ^2 values on the order of 10^{-6} .

Histograms of path lengths are plotted in Figure 2.7; the range of travel angles included in each plot is 0.1π , visualized by the black arrows. Due to the symmetry of the initial

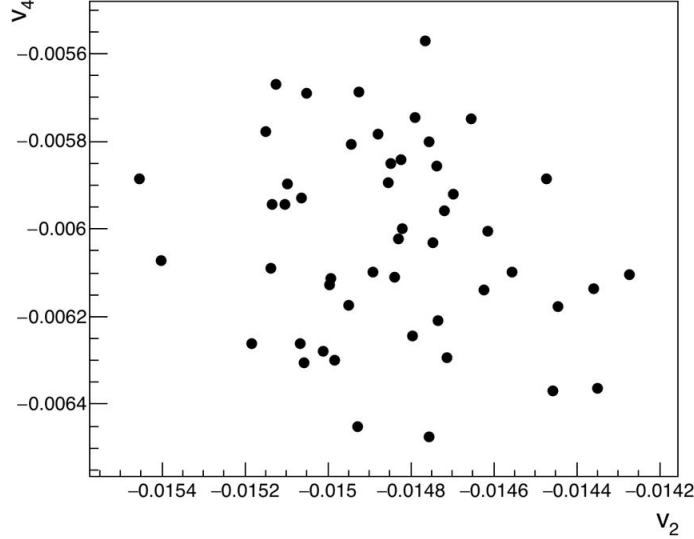


Figure 2.6: Values of v_2 and v_4 displayed no correlation (in this plot $\lambda = 0.5$; data from 50 runs are plotted).

distribution, the $\pi/2$ range covered by these plots is enough to understand the behavior of the whole system; this is evident in the plots for $-0.6\pi < \phi < -0.5\pi$ and $-0.5\pi < \phi < -0.4\pi$ in the reversal of the contributions from $x_0 < 0$ and $x_0 > 0$. Most importantly, the particles traveling at angles more parallel to the minor axis of the medium had shorter path lengths, which means they were more likely to escape the medium without collisions, confirming the presence of a differential escape probability.

2.5 Discussion

While these results show that differential particle survival can produce a higher-order flow harmonic, v_4 , from initial conditions with only elliptical eccentricity present, the low magnitude of the effect means that it cannot explain v_4 production on its own. Measurements at RHIC show a quadratic relationship between v_2 and v_4 , which was not produced by this model; in contrast, hydrodynamic models are able to explain the relationships in RHIC data up to a factor of two.

Previously it was believed that partons scattering off one another led to the generation of harmonics, which makes sense in the hydrodynamic limit of many scatterings. However, this was disproven with the discovery that in models such as AMPT, most particles in small systems do not undergo any scattering [47]. In 2016, He et al. showed that the evolution of

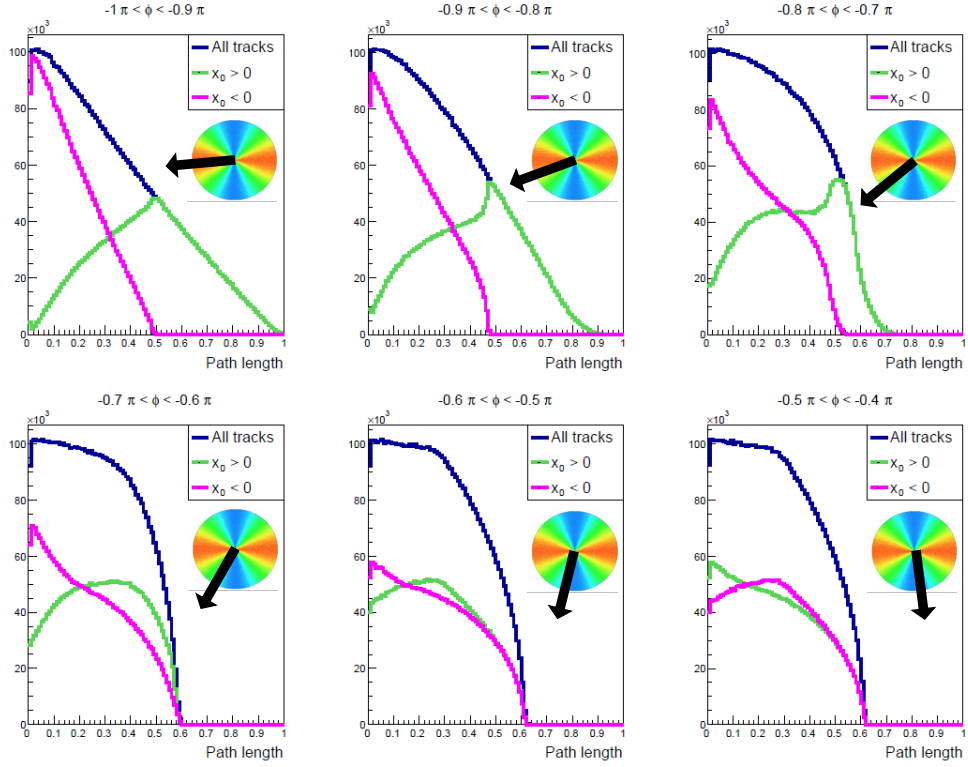


Figure 2.7: Histograms of path length; each plot is made up of particles with travel angles ϕ ranging over 0.1π . The green line shows particles starting in the right half of the medium ($x_0 > 0$), magenta shows particles starting from the left half ($x_0 < 0$), and the blue line is their sum. As expected, particles travelling predominantly through the less dense portions of the region had the shorter path lengths, and thus higher survival.

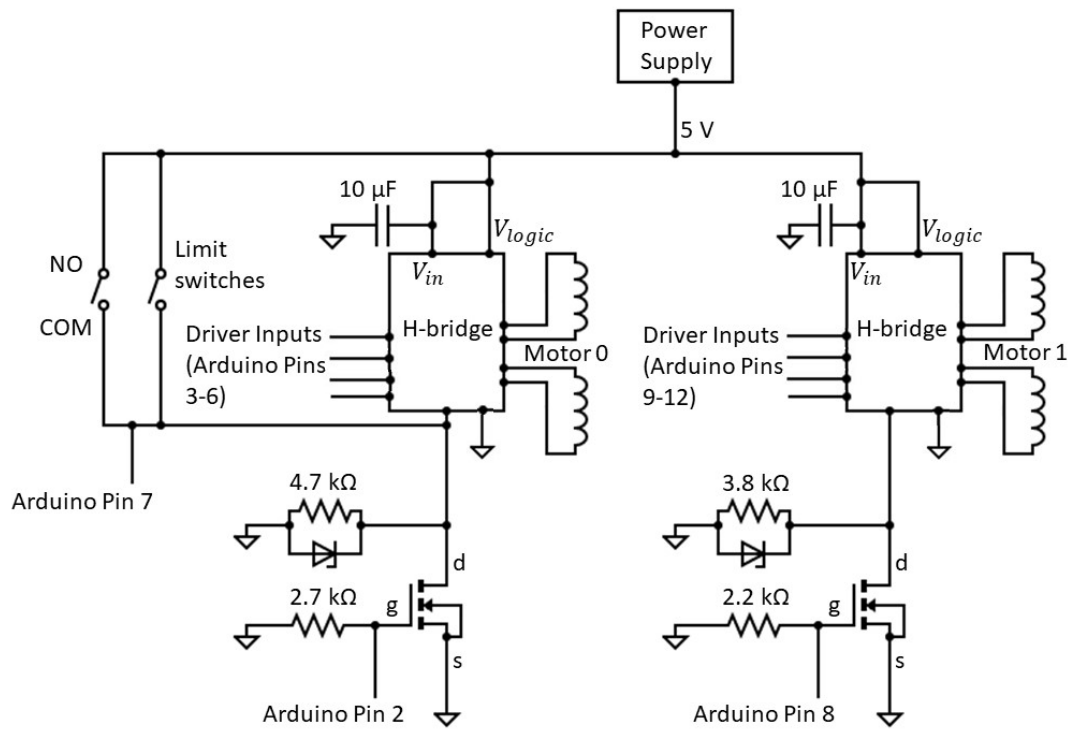
a v_2 in elliptically eccentric collisions was due to the higher likelihood of particles escaping along the minor axis of the ellipse [41]. These particles were more likely to freeze out without experiencing any collisions because they had to travel through less of the medium. The authors note that any contribution to v_2 from multiple collisions was minor. They also show the same effect leads to v_3 production and speculate that this is the mechanism by which all flow harmonics in particle transport models are produced.

The present work shows that differential escape probability can produce a non-zero v_4 from a distribution with an initial ε_4 equal to zero. In this model, weighting by the survival function (2.6) is used as a proxy for the number of collisions a particle undergoes, with a higher weight corresponding to fewer collisions. When examining which particles were more likely to escape as a function of travel angle, it was clear that the more parallel a particle's path was to the minor axis of the medium, the more likely it was to escape (Figure 2.7); this shows that the differential escape probability was in fact the mechanism responsible for the development of a v_4 . Because the particles that did scatter were not considered, the model shows the effects of differential survival alone, without any compounding effects from multiple collisions. The density of the medium and its transparency—how easily a particle can pass through without being diverted—were both tunable through the total number of particles used (N) and a parameter in the survival function (λ), respectively. The non-zero v_4 present with all tested values of these parameters suggests that the effect is present across system sizes.

The model presented here assumes no inter-particle interaction beyond absorption, but does not account for the effects of scattering. It assumes all partons in the medium are identical and that there is an abrupt and absolute edge to the medium. To further test this model, studies in a comprehensive particle model such as AMPT should be carried out in the manner of reference [41]. Modeling under more realistic conditions would create a more accurate result; however, a simplified model such as this is valuable because by nature it can only show a certain number of effects, limiting the number of things which can interact and making the underlying mechanisms easier to identify.

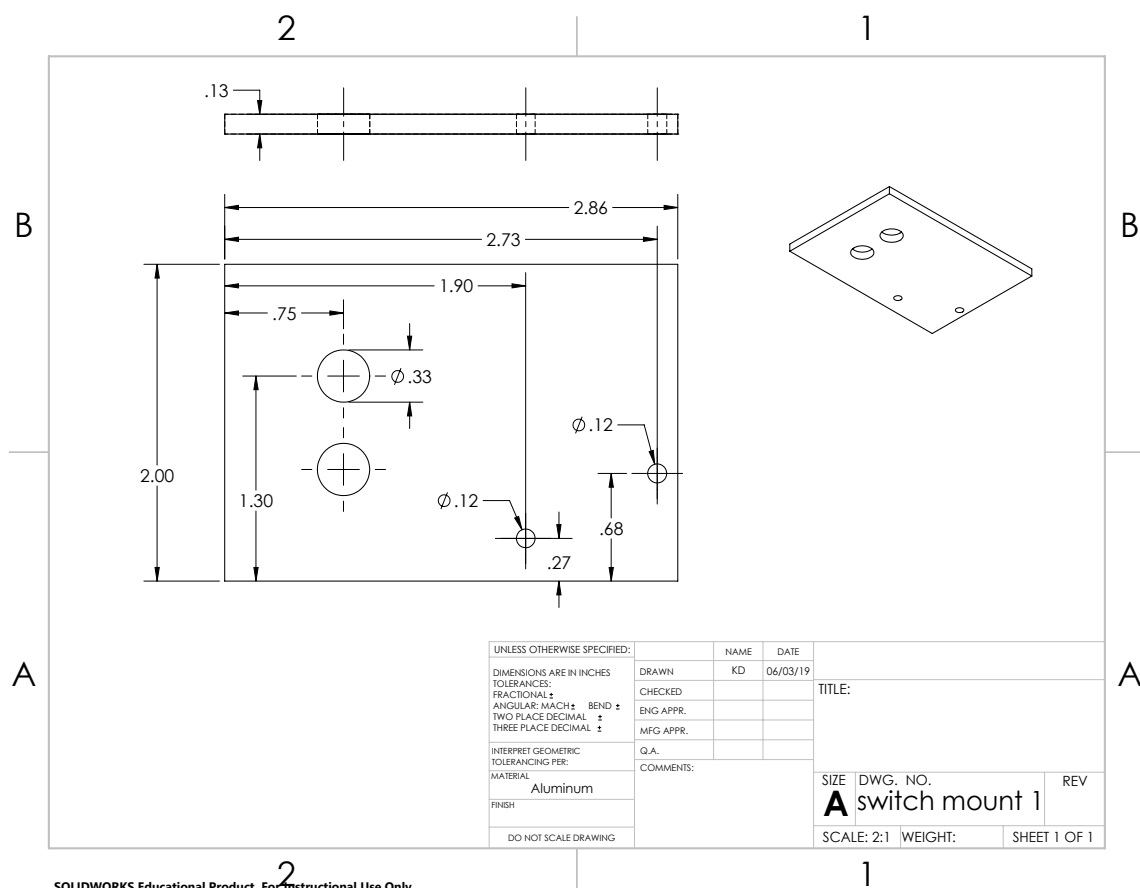
Appendix A

Circuit Diagram

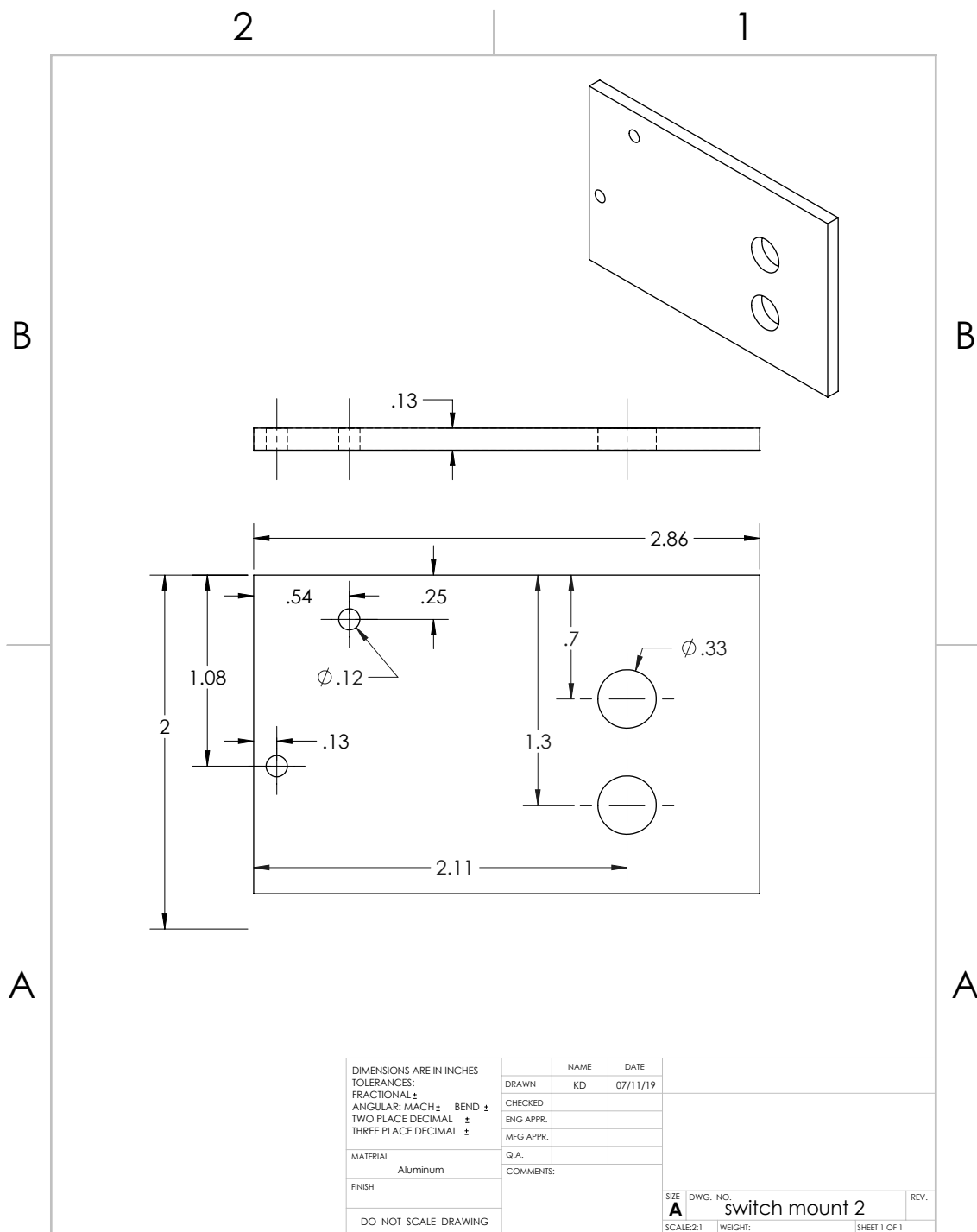


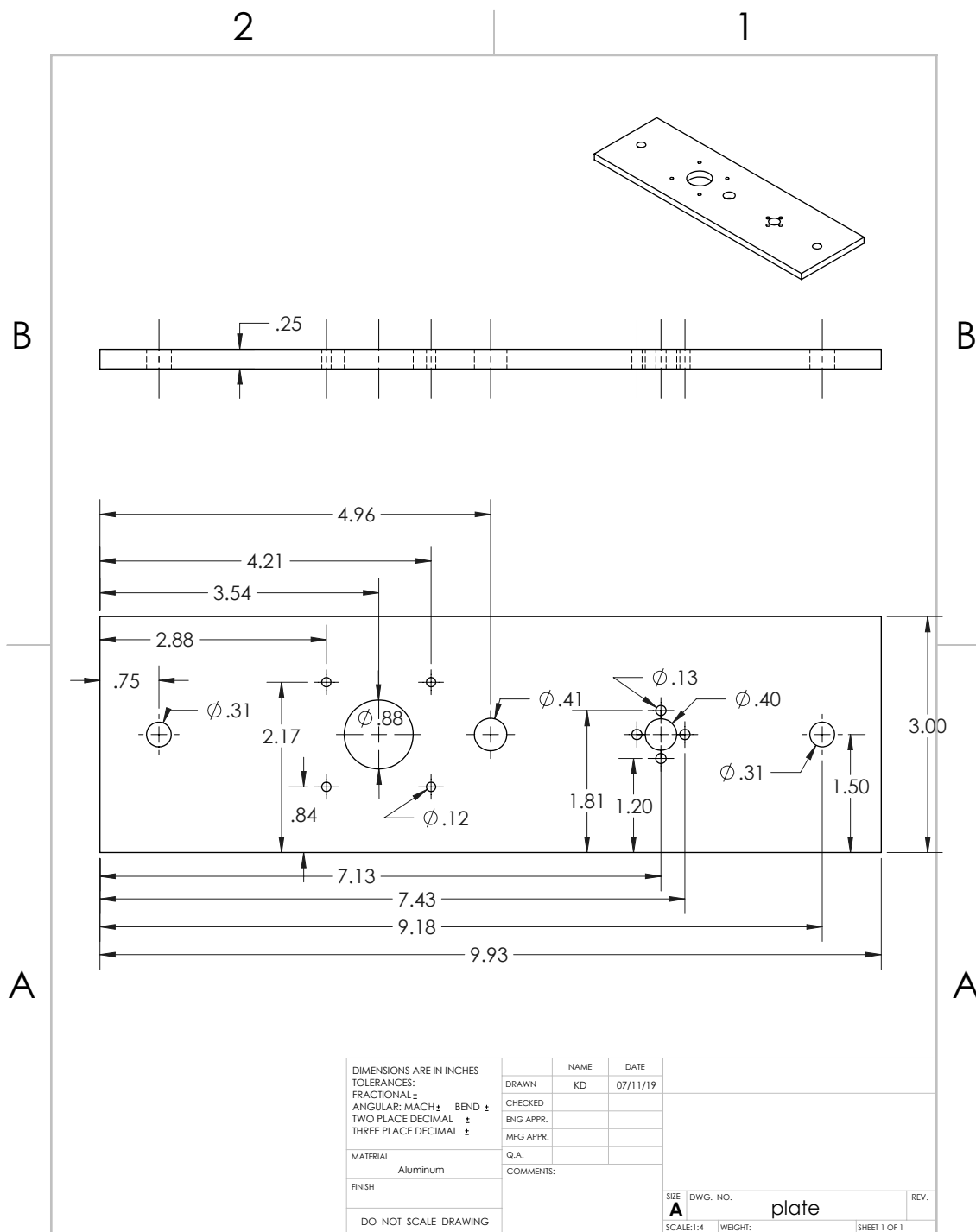
Appendix B

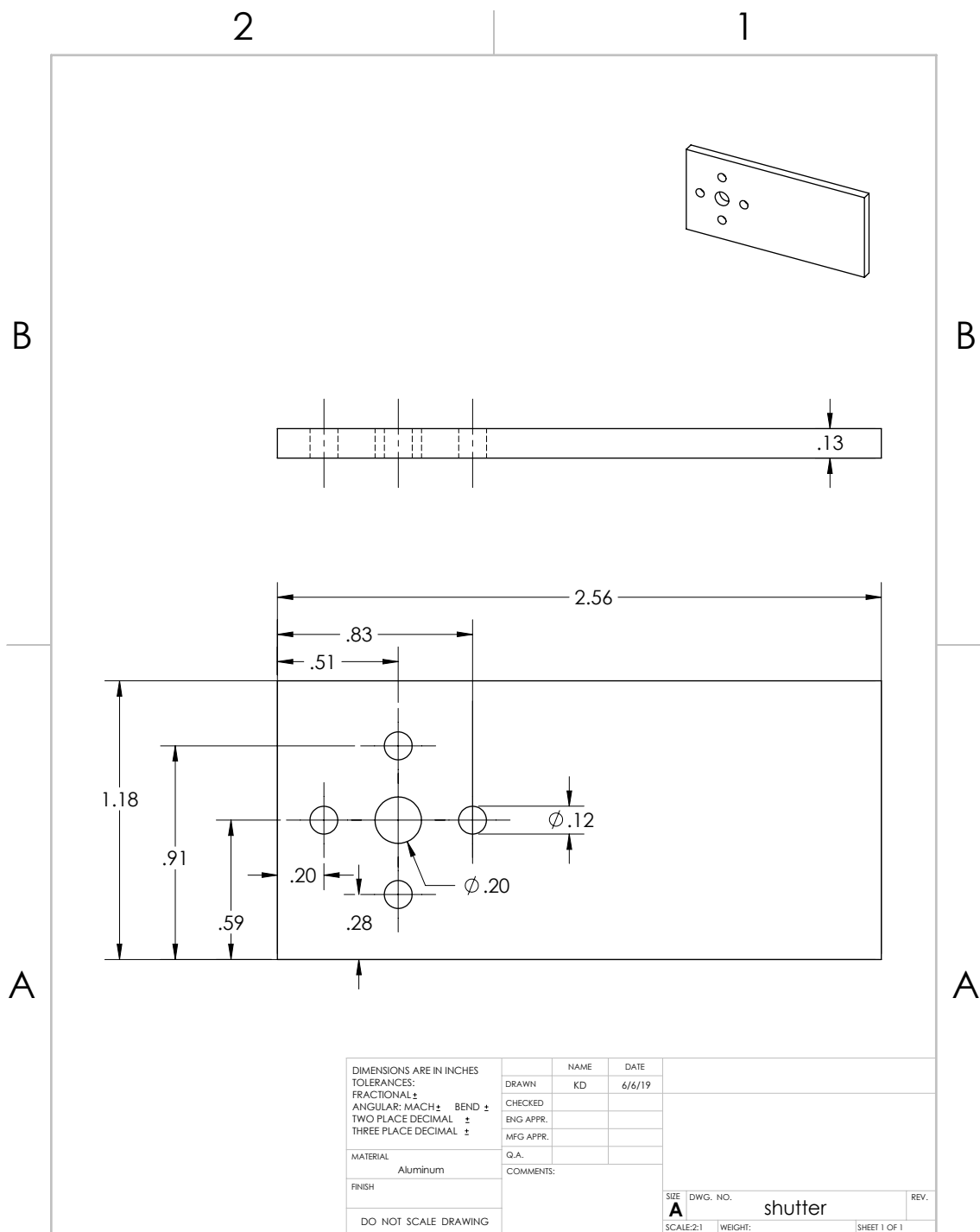
Drawings

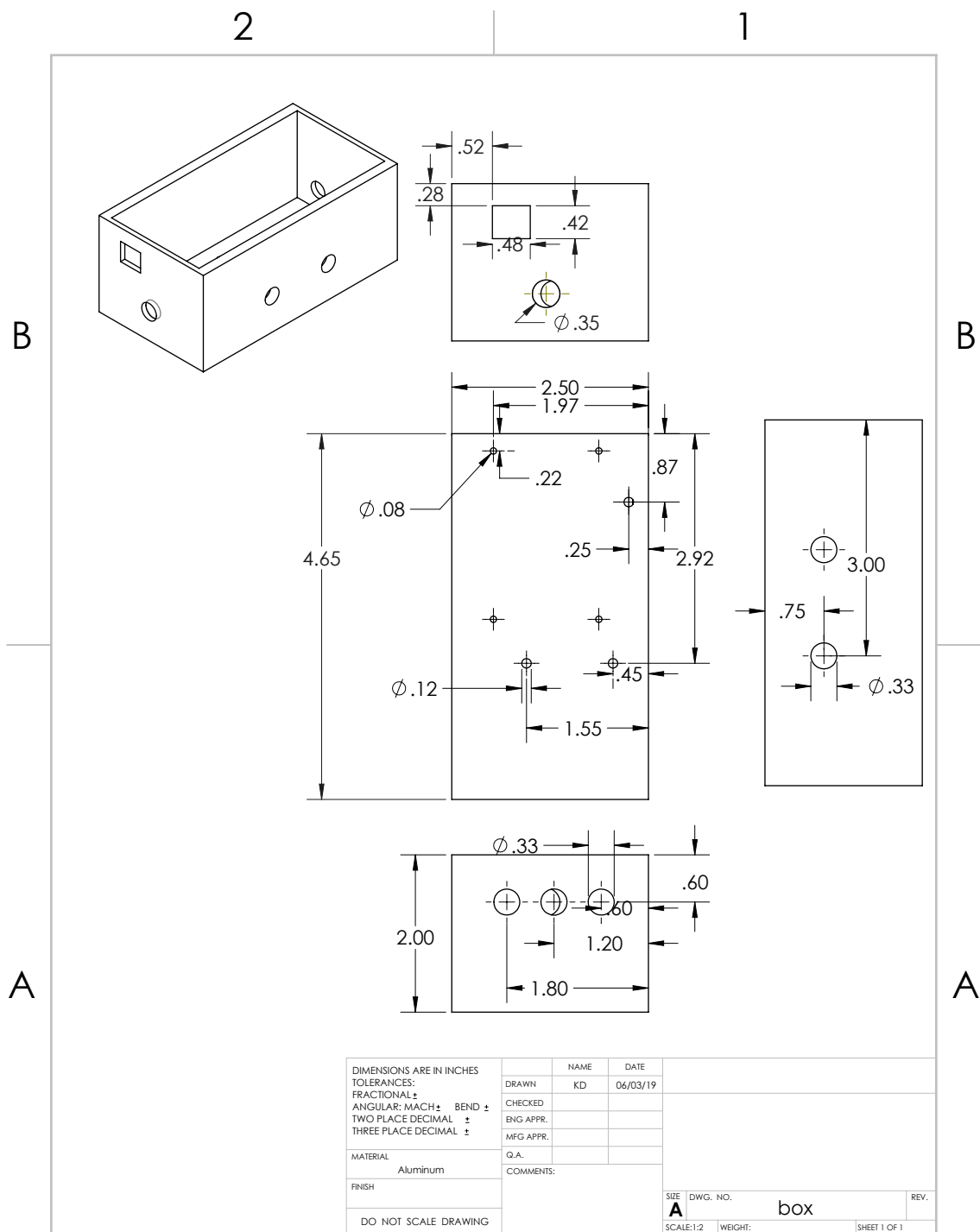


SOLIDWORKS Educational Product. For Instructional Use Only.









Appendix C

Instructions

C.1 Assembly

- Tools required: $\frac{3}{16}$ " hex key, $\frac{5}{32}$ " hex key, M2 hex key, Philips screw driver for M3 screws, level (recommended), soldering supplies
- General notes: A list of parts and an assembly diagram with part numbers can be found in Appendices C.1.1 and C.1.2, respectively. To attach brackets, put bolts through each hole in the bracket. Loosely attach nut and slide into desired slot, then tighten. Bolts use $\frac{3}{16}$ " hex key unless noted.

I. Platform:

- A. Attach lead screw nut (11) to platform (21) using 4 M3x16 flathead screws and nuts.
- B. Attach 3" (7.62 cm) T-slot (17) to ends of platform using T-nuts, on same face of platform as lead screw nut. T-slot and platform should be aligned but don't need to be exact.
- C. Using $\frac{5}{32}$ " hex key, attach vertical face of T-slot to bolts on wheel assembly (4). Wheels should be facing outward. On one side of the platform there is a line marked through the center of the plate; this should be aligned with the lines marking the centers of the wheel assemblies.
- D. On the same side as the lead screw nut, secure NEMA 17 motor (14) to platform using M3x12 flathead screws, with wires facing nearest set of wheels.

- E. Attach NEMA 17 coupler (15) to shutter (16) using M3x12 flathead screws and nuts. Mount shutter on motor shaft using included hex key to tighten set screws.

II. Base:

- A. Attach limit switches (23) to switch mounts (24 & 25) using 4 black M3x20 bolts and nuts (red side of switch facing outward). On switch mount 2 (25), the set of holes along the short edge should be used to mount the switch.
- B. Place 2 T-nuts and bolts onto mount. On one piece of 7.87" (20 cm) T-slot (19), secure limit switch mount 2 in the center so the lever is on top.
- C. Attach 2 brackets (8) to each of the single-thickness pieces of 7.87" (20 cm) T-slot, on the same face and with one on each end. The piece with the switch should have the brackets attached to the same face as the switch.
- D. Slide 7.87" (20 cm) double-thickness T-slot (20) pieces into the brackets on the thin pieces, forming a rectangle. The cut end of thin T-slot should be against the narrow side of the wide T-slot, and markings on wide pieces should be facing up and on same side of rectangle.
- E. Tighten bolts well; the levelness of the base affects how well the vertical posts are aligned.

III. Upper Frame:

- A. Attach 2 brackets on one end of each 16.54" (42 cm) T-slot side post (1) on opposite faces. Place one on each side on the outer rail of double wide T-slot, aligning with markings on base. Use a level to ensure the posts are vertical.
- B. Slide platform wheel-side up onto vertical posts with NEMA 17 motor and shutter on right side.
- C. Slide switch mount 1 (24) onto back of right post so that lever will contact platform. Do not tighten bolts.
- D. Attach one bracket on the inside of the top end of each post, with the open face of the bracket in the plane of the cut face of the post.
- E. Slide 13.88" (35.25 cm) crossbar (18) onto top of posts. Ensure marking for motor mount is on the front face of crossbar. Do not tighten bolts.
- F. Tighten bolt on one side of the crossbar. Adjust the position of the other bracket so that the plate glides smoothly (this may take several tries). Tighten remaining side.
- G. Place lead screw (13) into nut attached to platform.

IV. NEMA 23 Motor:

- A. Attach narrow end of coupler (12) to NEMA 23 motor shaft (10) using M2 hex key for the set screws. Tighten well; if the set screws are too loose, the coupler can gradually slip down the motor shaft while the platform is moving.
- B. Place one bolt through the top of each slot in NEMA 23 motor mount (9), attaching a square nut on reverse. Do not tighten fully.
- C. Place one T-nut on each bolt and slide mount assembly into 4.5" (11.43 cm) T-slot (22). Center and tighten bolts so that mount edge is parallel with T-slot. The square nuts may need to be readjusted.
- D. Secure NEMA 23 motor in mount, with wires facing back, using M4x19 screws.
- E. Place a bracket on each side of the crossbar over the marking for T-slot with open faces down. Slide motor assembly onto these and center before tightening.
- F. Slide lead screw into coupler and tighten set screws using M2 hex key. Secure limit switch mount so that bottom of mount is level with bottom of coupler.

V. Finishing:

- A. Slide electronics box (2 & 3) into right double-thickness T-slot base, with T-nut inside the T-slot and the square nut between the T-slot and the box.
- B. Solder motor and switch wires to appropriate leads, making sure to leave enough wire for full range of vertical motion of NEMA 17.
- C. Secure wires to frame, making sure nothing is fastened around posts so that wheels can move freely.

C.1.1 List of Parts

Part name (part identification number):

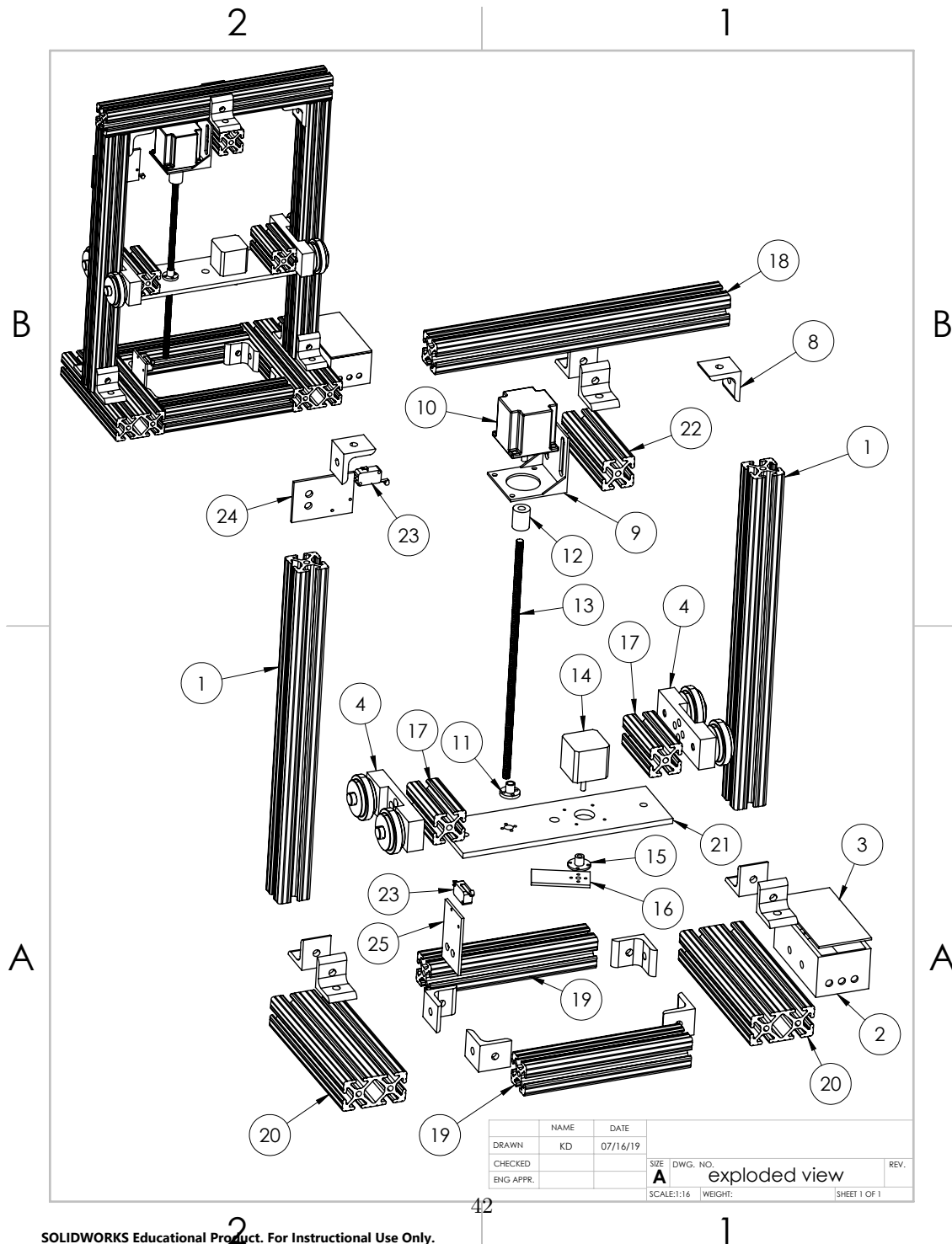
- 2 pieces 16.54" (42 cm) t-slot—side posts (1)
- 1 electronics box with lid (+2 T-nuts and bolts and 2 square nuts attached) (2 & 3)
- 2 wheel assemblies (each with 2 nuts and bolts attached) (4)
- 12 brackets (8)
- 1 NEMA 23 motor mount (9)
- 1 NEMA 23 motor (10)
- 1 lead screw nut (11)
- 1 flexible coupler (4 set screws inside) (12)
- 1 lead screw (13)
- 1 NEMA 17 motor (14)
- 1 coupler for NEMA 17 (2 set screws) inside (15)
- 1 shutter (16)
- 2 pieces 3" (7.62 cm) T-slot—wheel mounts (17)
- 1 piece 13.88" (35.25 cm) T-slot—crossbar (18)
- 2 pieces normal-wide 7.87" (20 cm) T-slot—inner base (19)
- 2 pieces double-wide 7.87" (20 cm) T-slot—outer base (20)
- 1 platform (21)
- 1 piece 4.5" (11.43 cm) T-slot—motor mount (22)
- 2 limit switches (23)
- 2 limit switch mounts (24 & 25)
- 1 USB cable

Fasteners:

- 32 T-nuts and bolts (+2 on electronics box)
- 2 square nuts (+2 on electronics box)
- 8 M3x12 flathead screws
- 4 black M3x20 hex socket screws
- 4 M3x16 flathead screws
- 4 M4x19 screws
- 16 M3 nuts
- 4 M4 nuts
- 4 bolts and nuts attached to wheel assemblies

C.1.2 Assembly Diagram

CAD models for Part 4, Part 8, and all T-slot components were downloaded from their manufacturer, 80/20 Inc. [50–53].



C.2 Use

- I. Install LabVIEW Interface for Arduino (LIFA) following the instructions here: <https://knowledge.ni.com/KnowledgeArticleDetails?id=kA00Z000000PAS1SA0&l=en-US>.
- II. Place radiation source on platform next to the NEMA 17 motor, over the hole. Ensure shutter is positioned under the hole with its sides parallel to the edges of the plate.
- III. Plug USB into square port on electronics box.
- IV. Connect PSU to banana jacks—high to red, low to black, ground to black (the black ones are connected internally).
- V. Turn PSU on and limit its output to 5 V and 1 A.
- VI. Open *Stepper System Control.vi* in LabVIEW.
- VII. Enter the serial port number of the USB connection in the “Serial Port” control.
- VIII. Start the program by clicking on the white arrow on the top left of the tool bar.
- IX. Click on any button to execute that function. If using the “Move” function, set desired speed (steps/sec) and distance (mm) to go.
- X. Exit the program by clicking the “Stop Program” button.
- XI. To add *Stepper System Control.vi* to existing code, refer to Part III of Appendix C.3. To make custom preset routines, refer to Appendix C.3.

Notes:

- The front panel locks when anything is executing. This is to prevent step-counting errors on the position indicator.
- When setting the “Distance To Go” indicator, positive values move the platform up and negative values move it down.
- If the current position isn’t zero when the program is opened but should be, it can be manually set by typing 0 into the “Current Position” indicator before running the program.
- Recommended speed: < 120 steps/sec

- The “Stop Program” button does not stop motion of the stepper; it is locked like the rest of the front panel when a function is executing. It is only meant to quit running the program. The coded limits on range of motion will prevent the device from moving beyond its bounds (in *Move sub.vi*). Should these be incorrect, shut off the power supply unit to stop motor.

C.3 Building Custom SubVIs

I. Build a state machine:

- A. Open a new block diagram and make a while loop.
- B. Add a case structure.
- C. Right-click on the while loop and select “Add shift register”. Add a total of two sets of shift registers.
- D. Create an enum and wire it to one shift register on the left.
- E. Right-click the enum and select “Edit items”.
- F. Add each state you need, one for each action including initialize and close. Order doesn’t matter, unless you want them in an order that is intuitive for the programmer to click through.
- G. Wire the left shift register (connected to the enum) to the question mark on the side of the case structure.
- H. Right-click the case structure and select “Add case for every value”.
- I. Copy and paste the original enum into the first state and change its value to whatever the next state should be. Wire it to the corresponding right shift register. If red coercion dots appear on the shift register, you may need to delete all enums except the original, then copy and paste them all again. This may happen if you add cases after you’ve already wired some.
- J. Repeat the previous step for each case. In the last case, wire the “Initialize” enum to the shift register.
- K. Add a true constant inside the last case and wire it to the stop button. Right-click on the tunnel and select “Use default if unwired”.

II. Add desired functions:

- A. On the front panel, place a VISA resource control, a Boolean control to start the program, and both an indicator and a control for current position.
- B. On the block diagram, place an event structure around the state machine. Right-click on the event, select “Edit events handled by this case”, and select the name of your Boolean button from the “Event Sources” menu.
- C. Wire the current position control to the unused left shift register, and the current position indicator to the corresponding shift register on the right.

- D. Add subVIs (e.g. *Move sub.vi* and *Turn sub.vi*) for desired functions to each case and wire constants to their inputs.
- E. Place setup sub.vi on the left of the diagram, outside the event, and wire it appropriately to each subVI in the diagram, including the VISA resource.
- F. Outside the event, on the right, place a *close.vi* wired to a *simple error handler.vi* (found in LabVIEW function menu; *close.vi* is in the Arduino section) for each set of Arduino wires. Wire the output of the subVI to these. If a case does not use a resource, connect its wires from the left to right tunnels. This prevents undesired default cases.
- G. Check that the finished program is working correctly.

III. Make into subVI:

- A. Highlight everything inside the event structure.
- B. From the menu at the top, go to “Edit” and select “Create subVI”.
- C. Save the main VI, which will prompt you to name and save the new subVI.
- D. Double-click the subVI icon to open its front panel. By right-clicking the icon in the upper right you can edit the icon.
- E. Terminal names can be edited on the front panel. It may be helpful to have the block diagram open to determine which terminals are which.
- F. To edit the location of terminals, you can choose a different pattern by right-clicking the icon with terminals. The go into the VI where it was created, right-click the subVI, and select “Re-link to SubVI”.
- G. In the front panel of the subVI, hold Control and then click two terminals to swap their locations. If the terminals do not auto-fill, click on a terminal and then the desired front panel object to connect them. De-select by clicking an empty part of the front panel.

IV. Call as event in main VI:

- A. On the front panel of *Stepper System Control.vi*, add a Boolean button to start the new preset function.
- B. In the block diagram of *Stepper System Control.vi*, add a new event case for this button.
- C. From the function menu, select the new subVI and place it in the event. Wire all terminals appropriately. If any tunnels in the event are unused, wire them through to prevent default cases.
- D. Test the new preset function.

Bibliography

1. *Discover — ATLAS Experiment at CERN* <https://atlas.cern/discover> (2019).
2. *High-Luminosity LHC — CERN* <https://home.cern/science/accelerators%20/high-luminosity-lhc> (2019).
3. Bhattacharya, P. *et al.* Performance studies of bulk Micromegas of different design parameters. *Journal of Instrumentation* **9**, C04037–C04037. ISSN: 1748-0221 (Apr. 2014).
4. Bhattacharya, D. S. *et al.* Experimental and numerical simulation of a TPC like set up for the measurement of ion backflow. *Nuclear Instruments and Methods in Physics Research Section A: Accelerators, Spectrometers, Detectors and Associated Equipment* **861**, 64–70. ISSN: 01689002 (July 2017).
5. Kuger, F. *et al.* Mesh geometry impact on Micromegas performance with an Exchangeable Mesh prototype. doi:10.1016/j.nima.2015.11.011. <http://dx.doi.org/10.1016/j.nima.2015.11.011> (2016).
6. Kato, Y. *et al.* Activity report of ILD-TPC Asia group in *International Workshop on Future Linear Colliders* (2014). arXiv: 1403.7717v1. <https://arxiv.org/abs/1403.7717>.
7. Abraamyan, K. *et al.* The MPD detector at the NICA heavy-ion collider at JINR. *Nuclear Instruments and Methods in Physics Research Section A: Accelerators, Spectrometers, Detectors and Associated Equipment* **628**, 99–102. ISSN: 01689002 (Feb. 2011).
8. Alexopoulos, T. *et al.* A spark-resistant bulk-micromegas chamber for high-rate applications. *Nuclear Instruments and Methods in Physics Research Section A: Accelerators, Spectrometers, Detectors and Associated Equipment* **640**, 110–118. ISSN: 01689002 (June 2011).

9. Sidiropoulou, O. *et al.* Performance studies under high irradiation and ageing properties of resistive bulk Micromegas chambers at the new CERN Gamma Irradiation Facility. *Nuclear Instruments and Methods in Physics Research Section A: Accelerators, Spectrometers, Detectors and Associated Equipment* **845**, 293–297. ISSN: 01689002 (Feb. 2017).
10. Giomataris, I. *High Rate Applications of Micromegas and Prospects* tech. rep. (2006). <https://arxiv.org/ftp/physics/papers/0610/0610153.pdf>.
11. Colas, P., Giomataris, I., Lepeltier, V. & Ronan, M. First test of a Micromegas TPC in a magnetic field. *Nuclear Instruments and Methods in Physics Research A* **535**, 181–185 (2004).
12. Giomataris, I. *et al.* Micromegas in a Bulk. *Nuclear Instruments and Methods in Physics Research Section A: Accelerators, Spectrometers, Detectors and Associated Equipment* **560**, 405–408 (2006).
13. Anthony, K. *Preparing ATLAS for the future — ATLAS Experiment at CERN* 2018. <https://atlas.cern/updates/atlas-news/preparing-ATLAS-for-future> (2019).
14. Vandenbroucke, M. Discharge reduction technologies for Micromegas detectors in high hadron flux environments. *Journal of In* **7**, C05014 (2012).
15. CMS Collaboration. *Measurement of higher-order harmonic flow in PbPb collisions at $\sqrt{s} \text{ NN} = 2.76 \text{ TeV}$* tech. rep. (2011). <http://cds.cern.ch/record/1361385/files/HIN-11-005-pas.pdf>.
16. Fonte, P. & Peskov, V. On the physics and technology of gaseous particle detectors. *Plasma Sources Science and Technology* **19**, 034021 (2010).
17. Iodice, M. Micromegas detectors for the muon spectrometer upgrade of the ATLAS experiment. *Journal of Instrumentation* **10**, C02026 (2015).
18. Bhattacharya, D. S. *et al.* in, 505–507 (Springer, Cham, 2018). doi:10.1007/978-3-319-73171-1_118. http://link.springer.com/10.1007/978-3-319-73171-1_118.
19. Rout, P. K. *et al.* *Experimental Studies of Ion Backflow for a Bulk Micromegas Detector Using Various Argon-Based Gas Mixtures* in *Springer Proceedings in Physics* **201** (2017), 81–90. doi:10.1016/j.nima.2017.04.031. <http://www.springer.com/series/361>.
20. Nikolopoulos, K., Bhattacharya, P., Chernyatin, V. & Veenhof, R. Electron transparency of a Micromegas mesh. *Journal of Instrumentation* **6**, P06011–P06011. ISSN: 1748-0221 (June 2011).

21. Kaminski, J. *Micropattern Gas Detectors* in *17th International Workshop on Vertex Detectors* (2009), 38. <http://pos.sissa.it/>.
22. Bhattacharya, P. *et al.* Investigation of ion backflow in bulk micromegas detectors. *Journal of Instrumentation* **10**, P09017–P09017. ISSN: 1748-0221 (Sept. 2015).
23. Bortfeldt, J. *Development of Floating Strip Micromegas Detectors* doctoral (Ludwig-Maximilians-Universitaet Muenchen, 2014). https://edoc.ub.uni-muenchen.de/16972/1/Bortfeldt%7B%5C_%7DJonathan.pdf.
24. SOLIDWORKS 3D CAD Design Software. <https://www.solidworks.com/> (2019).
25. NEMA 23 stepper motor datasheet, Wantai Motor. <http://www.bc-robotics.com/wp-content/uploads/2016/04/57BYGH420-2.pdf>.
26. NEMA 17 stepper motor datasheet, StepperOnline. <https://www.omc-stepperonline.com/download/17HS16-2004S1.pdf>.
27. AMCI : Advanced Micro Controls Inc :: Stepper vs Servo <https://www.amci.com/industrial-automation-resources/plc-automation-tutorials/stepper-vs-servo/> (2019).
28. *How do stepper motors work? - Explain that Stuff* <https://www.explainthatstuff.com/how-stepper-motors-work%20.html> (2019).
29. *Types of Steppers — All About Stepper Motors — Adafruit Learning System* <https://learn.adafruit.com/all-about-stepper-motors/types-of-steppers> (2019).
30. *Iron-55 — Princeton University Office of Environmental Health and Safety* <https://ehs.princeton.edu/laboratory-research/radiation-safety/radioactive-materials/radioisotope-fact-sheets/iron-55> (2019).
31. *MOSFET as a Switch - Using Power MOSFET Switching* https://www.electronicstutorials.ws/transistor/tran%7B%5C_%7D7.html (2019).
32. Arduino Uno Rev3. <https://store.arduino.cc/usa/arduino-uno-rev3> (2019).
33. LabVIEW 2019 - National Instruments. <https://www.ni.com/en-us/shop/labview/labview-details.html> (2019).
34. *Miniature Basic Switch* tech. rep. (). https://media.digikey.com/pdf/Data%20Sheets/Omron%20PDFs/V%7B%5C_%7DMini%7B%5C_%7DBasic%7B%5C_%7DSwitch.pdf.
35. SN754410 SN754410 Quadruple Half-H Driver 1 Features 3 Description. www.ti.com (1986).
36. STMicroelectronics. *DUAL FULL-BRIDGE DRIVER* tech. rep. (2000). https://www.sparkfun.com/datasheets/Robotics/L298%7B%5C_%7DH%7B%5C_%7DBridge.pdf.

37. Franz, K. *What Is an H-Bridge?* – Digilent Inc. Blog <https://blog.digilentinc.com/what-is-an-h-bridge/> (2019).
38. QFET TM FQP30N06L FQP30N06L 60V LOGIC N-Channel MOSFET General Description. <https://cdn.sparkfun.com/datasheets/Components/General/FQP30N06L.pdf> (2001).
39. Archived: Installing LabVIEW Interface for Arduino Toolkit Using VI Package Manager - National Instruments. <https://knowledge.ni.com/KnowledgeArticleDetails?id=kA00Z000000PAS1SA0%7B%5C%7D1=en-US> (2019).
40. Busza, W., Rajagopal, K. & van der Schee, W. Heavy Ion Collisions: The Big Picture and the Big Questions. *Annual Review of Nuclear and Particle Science* **68**, 339–376. ISSN: 0163-8998 (Oct. 2018).
41. He, L. *et al.* Anisotropic parton escape is the dominant source of azimuthal anisotropy in transport models. *Physics Letters B* **753**, 506–510. ISSN: 03702693 (Feb. 2016).
42. *The Physics — ATLAS Experiment at CERN* <https://atlas.cern/discover/physics> (2019).
43. Gombeaud, C. & Ollitrault, J.-Y. Why is $v_4/(v_2)^2$ larger than predicted by hydrodynamics? 1. arXiv: 0910.0392v1. <https://arxiv.org/pdf/0910.0392v1.pdf> (2009).
44. Heinz, U. & Snellings, R. Collective Flow and Viscosity in Relativistic Heavy-Ion Collisions. doi:10.1146/annurev-nucl-102212-170540. www.annualreviews.org (2013).
45. Gardim, F. G., Grassi, F., Luzum, M. & Ollitrault, J.-Y. Mapping the hydrodynamic response to the initial geometry in heavy-ion collisions. *PHYSICAL REVIEW C* **85**, 24908 (2012).
46. Yan, L., Pal, S. & Ollitrault, J.-Y. *Nuclear Physics A Nonlinear hydrodynamic response confronts LHC data* tech. rep. (2018), 1–4. arXiv: 1601.00040v1. www.elsevier.com/locate/procedia.
47. Nagle, J. L. & Zajt, W. A. Small System Collectivity in Relativistic Hadronic and Nuclear Collisions. doi:10.1146/annurev-nucl-101916. <https://doi.org/10.1146/annurev-nucl-101916-> (2018).
48. Wei, D.-X., Huang, X.-G. & Yan, L. Hydrodynamic response in simulations within a multiphase transport model. *Physical Review C* **98**. doi:10.1103/PhysRevC.98.044908. <https://journals.aps.org/prc/pdf/10.1103/PhysRevC.98.044908> (2018).
49. ROOT a Data analysis Framework. <https://root.cern.ch/> (2019).

- 50. *2756* <https://8020.net/2756.html> (2019).
- 51. *1515* <https://8020.net/1515.html> (2019).
- 52. *1530* <https://8020.net/1530.html> (2019).
- 53. *45-4302* <https://8020.net/45-4302.html> (2019).